SIAM J. APPL. MATH.
Vol. 73, No. 6, pp. 2100–2123

DIMENSION REDUCTION OF THE SCHRÖDINGER EQUATION WITH COULOMB AND ANISOTROPIC CONFINING POTENTIALS*

WEIZHU BAO†, HUAIYU JIAN‡, NORBERT J. MAUSER§, AND YONG ZHANG¶

Abstract. We consider dimension reduction for the three-dimensional (3D) Schrödinger equation with the Coulomb interaction and an anisotropic confining potential to lower-dimensional models in the limit of infinitely strong confinement in one or two space dimensions and obtain formally the surface adiabatic model (SAM) or surface density model (SDM) in two dimensions (2D) and the line adiabatic model (LAM) in one dimension (1D). Efficient and accurate numerical methods for computing ground states and dynamics of the SAM, SDM, and LAM models are presented based on efficient and accurate numerical schemes for evaluating the effective potential in lower-dimensional models. They are applied to find numerically convergence and convergence rates for the dimension reduction from 3D to 2D and 3D to 1D in terms of ground state and dynamics, which confirm some existing analytical results for the dimension reduction in the literature. In particular, we explain and demonstrate that the standard Schrödinger–Poisson system in 2D is not appropriate to simulate a "2D electron gas" of point particles confined to a plane (or, more generally, a 2D manifold), whereas SDM should be the correct model to be used for describing the Coulomb interaction in 2D in which the square root of Laplacian operator is used instead of the Laplacian operator. Finally, we report ground states and dynamics of the SAM and SDM in 2D and LAM in 1D under different setups.

Key words. nonlinear Schrödinger equation, Coulomb interaction, Schrödinger–Poisson system, low-dimensional quantum systems, dimension reduction, anisotropic confining potential

AMS subject classifications. 35Q55, 65N35, 65T40, 65T50, 81-08

DOI. 10.1137/13091436X

1. Introduction.

Quantum systems of interacting (nonrelativistic) fermions or bosons can be "exactly" modeled by the linear N-particle Schrödinger equation under a proper given binary interaction potential (e.g., Coulomb) with each particle in three spatial dimensions (3D). Since this system is numerically intractable, usually effective "one particle" models are used, by using approximations like the Hartree(–Fock) ansatz and mean field theory [2, 13, 14, 15, 28, 29, 30, 32, 41, 45]. Thus, the original $3N$- or $3N+1$-dimensional problem (stationary or time-dependent) can be reduced to one or a coupled system of nonlinear Schrödinger (NLS) equation(s) in

*Received by the editors March 25, 2013; accepted for publication (in revised form) September 6, 2013; published electronically November 14, 2013.
http://www.siam.org/journals/siap/73-6/91436.html

†Department of Mathematics and Center for Computational Science and Engineering, National University of Singapore, Singapore 119076 (matbaowz@nus.edu.sg). This author's work was supported by the Singapore A*STAR SERC PSF grant 1321202067.

‡Department of Mathematical Sciences, Tsinghua University, Beijing, 100084, People's Republic of China (hjian@math.tsinghua.edu.cn). This author's work was supported by the National Natural Science Foundation of China through grant NSFC11271118 and by the Doctoral Programme Foundation of Institution of Higher Education of China.

§Wolfgang Pauli Institute, Fak. Mathematik, University Wien, 1090 Vienna, Austria (norbert.mauser@univie.ac.at). This author's work was supported by the Austrian Science Foundation (FWF) under grant F41 (project VICOM), grant I830 (project LODIQUAS), and grant W1245 and by the Austrian Ministry of Science and Research via its grant for the WPI.

¶Department of Mathematical Sciences, Tsinghua University, Beijing, 100084, People's Republic of China, and Wolfgang Pauli Institute, Fak. Mathematik, University Wien, 1090 Vienna, Austria (yong.zhang@univie.ac.at). This author's work was supported by the National Natural Science Foundation of China through grant NSFC11271118, by the Doctoral Programme Foundation of Institution of Higher Education of China, by the Austrian Science Foundation (FWF) under grant F41 (project VICOM), grant I830 (project LODIQUAS), and grant W1245, and by the Austrian Ministry of Science and Research via its grant for the WPI.

3D [13, 14, 15, 28, 29, 36]. In some situations, the 3D "one particle" NLS equation can be further reduced to lower-dimensional NLS equations in one or two space dimensions (1D or 2D), which decreases the numerical effort once more. The dimension reduction results from either a geometrical symmetry (e.g., a translational invariance in 1D or 2D) or confining the quantum particles in either one dimension (e.g., 2D "electron sheets") or two dimensions (e.g., 1D "quantum wires") or even all three space dimensions (0D "quantum dots") [16, 34, 43]. In fact, the confinement can be modeled by adding to the Hamiltonian operator an exterior confining potential with a small parameter, e.g., an anisotropic harmonic oscillator potential [17, 19, 20]. The small parameter limit of infinitely strong confinement then yields the correct asymptotic model in lower dimensions. In deriving and/or justifying rigorously mathematical models for low-dimensional quantum systems of fermions or bosons, physical intuition, asymptotic analysis, and numerical simulation play essential roles.

For bosons, especially Bose–Einstein condensation (BEC) [2, 41], by using a Hartree ansatz, the linear Schrödinger equation for N bosons under the short-range Fermi (or contact) interaction is well approximated by the Gross–Pitaevskii equation (GPE) in 3D which is an NLS equation with cubic nonlinearity [9, 20, 41]. Rigorous mathematical justification for this reduction can be found in the literature [5, 28, 35, 36, 37] for the ground state and dynamics of BEC. In addition, the 3D GPE for BEC is further dimensionally reduced to 2D and 1D GPEs for disk-shaped and cigar-shaped BECs, respectively, under anisotropic harmonic oscillator potentials [18]. Recently, dimension reduction for 3D GPEs to lower dimensions was extended to 3D GPEs with long-range dipole-dipole interaction for dipolar BEC with arbitrary dipolar polarization angles [22, 44]. For formal derivation of these dimension reduction and their mathematical justification and numerical comparison, we refer the reader to [4, 8] and references therein.

For electrons, again via the "mean field limit" [13, 14, 15, 29], the linear Schrödinger equation for N electrons with binary Coulomb interaction between different electrons can be approximated by a dimensionless single NLS equation with Coulomb interaction in 3D:

$$i\,\partial_t\psi(\mathbf{x},t) = \left[-\frac{1}{2}\Delta + V(\mathbf{x}) + \kappa\,\varphi\right]\psi, \qquad \mathbf{x}\in\mathbb{R}^3, \quad t>0, \tag{1.1}$$

where

$$\varphi(\mathbf{x},t) = \frac{1}{4\pi|\mathbf{x}|} * |\psi|^2 \quad \Longleftrightarrow \quad -\Delta\varphi(\mathbf{x},t) = |\psi(\mathbf{x},t)|^2, \qquad \mathbf{x}\in\mathbb{R}^3, \quad t\geq 0. \tag{1.2}$$

Here $\mathbf{x} = (x,y,z) \in \mathbb{R}^3$ is the spatial Cartesian coordinates, $\psi = \psi(\mathbf{x},t)$ is the complex-valued wave-function describing the electron system in a mean field approximation, $V(\mathbf{x})$ is a given real-valued external potential, φ is the Coulomb potential which is a convolution of the Coulomb kernel, i.e., $\frac{1}{4\pi|\mathbf{x}|}$, which happens to be the Green's function of the Laplace operator in 3D and the density $|\psi|^2$, and κ is a dimensionless coupling constant—the "Poisson coupling constant." Thus the system of (1.1)–(1.2) is usually called the Schrödinger–Poisson system (SPS) in the literature [12, 50]. In fact, the corresponding rigorous derivation of this kind of "Hartree equations" was started from a Hartree ansatz for the many-body (e.g., N-body) wave-function by using a "weak coupling scaling" (i.e., a factor 1/N in front of the Coulomb interaction potential) and passing to the limit $N\to\infty$ in the BBGKY hierarchy [13, 14, 29]. For detailed derivation of the above SPS (1.1)–(1.2) and its

mathematical justification, we refer the reader to [13, 14, 29] and references therein. In addition, by assuming uniform distribution of the electrons in one or two spatial dimensions and integrating the Coulomb interaction kernel $\frac{1}{4\pi|\mathbf{x}|}$ in 3D along the z-line or the (y,z)-plane, the SPS (1.1)–(1.2) in 3D can be further reduced to an SPS in 2D and 1D, respectively,

$$i\,\partial_t\psi(\mathbf{x},t) = \left[-\frac{1}{2}\Delta + V(\mathbf{x}) + \kappa\,\varphi\right]\psi, \qquad \mathbf{x}\in\mathbb{R}^d, \quad t>0, \tag{1.3}$$

$$-\Delta\varphi(\mathbf{x},t) = |\psi(\mathbf{x},t)|^2 \iff \varphi(\mathbf{x},t) = U_d(\mathbf{x}) * |\psi|^2, \quad \mathbf{x}\in\mathbb{R}^d,\ t\geq 0, \tag{1.4}$$

where $\mathbf{x} = x\in\mathbb{R}$ in 1D with $d=1$ and $\mathbf{x}=(x,y)\in\mathbb{R}^2$ in 2D with $d=2$, and U_d is the Green's function of the Laplace operator in d-dimensions defined as

$$U_d(\mathbf{x}) = \begin{cases} -\frac{1}{2}|\mathbf{x}|, & d=1,\\ -\frac{1}{2\pi}\ln|\mathbf{x}|, & d=2,\\ \frac{1}{4\pi}|\mathbf{x}|^{-1}, & d=3, \end{cases} \iff \widehat{U}_d(\xi) = \frac{1}{(2\pi)^{d/2}}\,\frac{1}{|\xi|^2}, \qquad \mathbf{x},\xi\in\mathbb{R}^d, \tag{1.5}$$

where $\widehat{f}(\xi)$ is the Fourier transform of a function $f(\mathbf{x})$ for $\mathbf{x},\xi\in\mathbb{R}^d$, which is defined as $\widehat{f}(\xi) = \frac{1}{(2\pi)^{d/2}}\int_{\mathbb{R}^d} f(\mathbf{x})\,e^{-i\xi\cdot\mathbf{x}}\mathrm{d}\mathbf{x}$.

Another way to reduce the SPS (1.1)–(1.2) in 3D to lower spatial dimensions is through applying strong confinement in one or two spatial dimensions. In fact, the spatial confinement is an essential feature of many "nanoscale devices" and has gained much attention from both experimental and mathematical studies [3, 31, 40, 42]. Although the SPS (1.3)–(1.4) in 2D or 1D has been used in some of the literature [1, 3, 12, 25, 27, 42, 43, 48, 50] to simulate low-dimensional quantum systems of fermions such as 2D "electron sheets" or 1D "quantum wires," it is highly debated or mathematically mysterious whether the above SPS is an appropriate model for these confining low-dimensional quantum systems. In fact, intuitively point particles confined to a 2D manifold still interact with the Coulomb interaction potential at $O\big(\frac{1}{|\mathbf{x}|}\big)$ in 2D; thus it seems that the SPS (1.3)–(1.4) in 2D is not an appropriate model. There have been some studies on finding appropriate mathematical models and providing mathematical and/or numerical justification for the quantum degenerated electron gas (degenerated Fermi gas) occurring in semiconductor devices due to the anisotropic confining potential [40]. Two asymptotic quantum transport models for 2D electron gas, namely, the SAM and the SDM, have been proposed from the SPS (1.1)–(1.2) in 3D by applying strong confinement in 1D [19, 40]. In addition, by using an interesting scaling in the 3D SPS (1.1)–(1.2), i.e., rescaling κ in an appropriate way to the confinement strength, the NLS equation with cubic nonlinearity in 1D was obtained [17].

The main aim of this paper is to derive asymptotically and systematically dimension reduction of the 3D SPS (1.1)–(1.2) under an anisotropic confining potential to lower-dimensional models in the limit of infinitely strong confinement in one or two spatial dimensions and to provide numerical and/or mathematical justification for this dimension reduction. For this purpose, we take the anisotropic confining potential $V(\mathbf{x})$ in (1.1) of the following forms with $\mathbf{x}_\perp = (x,y)\in\mathbb{R}^2$ and $\mathbf{x} = (\mathbf{x}_\perp, z)\in\mathbb{R}^3$:

Case I (pancake-shaped). The potential is strongly confined in the vertical z-direction as

$$V(\mathbf{x}) = V_2(\mathbf{x}_\perp) + \frac{1}{\varepsilon^2}V_z\left(\frac{z}{\varepsilon}\right), \quad \mathbf{x}\in\mathbb{R}^3, \qquad \text{satisfying} \quad \lim_{|z|\to\infty} V_z(z) = \infty. \tag{1.6}$$

Case II (cigar-shaped). The potential is strongly confined in the $\mathbf{x}_\perp$-plane as

$$V(\mathbf{x}) = V_1(z) + \frac{1}{\varepsilon^2} V_\perp\left(\frac{\mathbf{x}_\perp}{\varepsilon}\right), \quad \mathbf{x} \in \mathbb{R}^3, \qquad \text{satisfying} \quad \lim_{|\mathbf{x}_\perp|\to\infty} V_\perp(\mathbf{x}_\perp) = \infty. \tag{1.7}$$

In both cases, $0 < \varepsilon \ll 1$ is a small dimensionless parameter describing the strength of the confinement. In Case I, when $\varepsilon \to 0^+$, the 3D SPS (1.1)–(1.2) can be reduced to a *surface adiabatic model* (SAM) or *surface density model* (SDM) in 2D, and, respectively, in Case II, it can be reduced to a *line adiabatic model* (LAM) in 1D. Numerical methods are presented for discretizing the SAM and SDM in 2D and LAM in 1D. Based on the numerical methods, the dimension reduction is studied numerically and the convergence rates are obtained from the numerical results. Comparisons with the SPS (1.3)–(1.4) in 2D and 1D are reported numerically. In addition, the SAM and SDM in 2D and LAM in 1D are applied to simulate low-dimensional quantum systems of electrons such as "electron sheets" or graphene in 2D or "quantum wires" in 1D.

The paper is organized as follows. In section 2, dimension reduction is presented in detail for the 3D SPS (1.1)–(1.2) to 2D and 1D when the potential is chosen as described in Cases I and II, respectively. In section 3, numerical methods are proposed for discretizing the SAM and SDM in 2D and LAM in 1D. Extensive numerical results are reported to confirm the dimension reduction and to show convergence rates and applications in section 4. Finally, some concluding remarks are drawn in section 5.

2. Derivation of low-dimensional models. In this section, we will present detailed dimension reduction for the 3D SPS (1.1)–(1.2) to 2D and 1D. Assume the initial data for the 3D SPS is given as

$$\psi(\mathbf{x}, 0) = \psi_0(\mathbf{x}), \qquad \mathbf{x} \in \mathbb{R}^3. \tag{2.1}$$

Define the linear operator H as

$$H = -\frac{1}{2}\Delta + V(\mathbf{x}), \qquad \mathbf{x} \in \mathbb{R}^3. \tag{2.2}$$

2.1. From 3D to 2D. When the potential $V(\mathbf{x})$ in (1.1) is chosen as Case I (1.6), then the linear operator H can be split as

$$H = -\frac{1}{2}\Delta_\perp + V_2(\mathbf{x}_\perp) - \frac{1}{2}\partial_{zz} + \frac{1}{\varepsilon^2} V_z\left(\frac{z}{\varepsilon}\right) := H_\perp + H_z^\varepsilon = H_\perp + \frac{1}{\varepsilon^2} H_{\tilde{z}}, \tag{2.3}$$

where $\Delta_\perp = \partial_{xx} + \partial_{yy}$, $z = \varepsilon\tilde{z}$ and

$$H_z^\varepsilon := -\frac{1}{2}\partial_{zz} + \frac{1}{\varepsilon^2} V_z\left(\frac{z}{\varepsilon}\right) = \frac{1}{\varepsilon^2}\left[-\frac{1}{2}\partial_{\tilde{z}\tilde{z}} + V_z\left(\tilde{z}\right)\right] := \frac{1}{\varepsilon^2} H_{\tilde{z}}, \tag{2.4}$$

$$H_\perp := -\frac{1}{2}\Delta_\perp + V_2(\mathbf{x}_\perp), \qquad H_{\tilde{z}} := -\frac{1}{2}\partial_{\tilde{z}\tilde{z}} + V_z\left(\tilde{z}\right). \tag{2.5}$$

For $H_{\tilde{z}}$ in (2.5), due to (1.6), we know that the following eigenvalue problem admits distinct orthonormal eigenfunctions:

$$H_{\tilde{z}}\chi(\tilde{z}) = \left[-\frac{1}{2}\partial_{\tilde{z}\tilde{z}} + V_z\left(\tilde{z}\right)\right]\chi(\tilde{z}) = \mu\chi(\tilde{z}), \qquad \tilde{z} \in \mathbb{R}, \tag{2.6}$$

with $\|\chi\|^2 := \int_{\mathbb{R}} |\chi(\tilde{z})|^2 \, \mathrm{d}\tilde{z} = 1$. In fact, they can be chosen to form an orthogonal basis of $L^2(\mathbb{R})$ and be denoted as $\{\chi_k(\tilde{z})\}$ with corresponding eigenvalues $\{\mu_k\}$ satisfying $\mu_0 < \mu_1 \leq \mu_2 \leq \cdots$. Thus $(\chi_k^\varepsilon(z), \mu_k^\varepsilon)$ with

$$\mu_k^\varepsilon = \frac{\mu_k}{\varepsilon^2}, \qquad \chi_k^\varepsilon(z) = \frac{1}{\sqrt{\varepsilon}}\chi_k(\tilde{z}) = \frac{1}{\sqrt{\varepsilon}}\chi_k\left(\frac{z}{\varepsilon}\right), \qquad k = 0, 1, 2, \ldots, \tag{2.7}$$

are orthonormal eigenpairs to the operator H_z^ε.

For simplicity of notation, here we only consider the "pure state" case in the strong confinement direction, especially the "ground state" case [19, 20]. Assuming that the initial data ψ_0 in (2.1) satisfies

$$\psi_0(\mathbf{x}) \approx \psi_2(\mathbf{x}_\perp)\chi_0^\varepsilon(z), \qquad \mathbf{x} \in \mathbb{R}^3, \qquad 0 < \varepsilon \ll 1, \tag{2.8}$$

noting the scale separation in (2.3), when $\varepsilon \to 0^+$, the solution ψ to the 3D SPS (1.1)–(1.2) can be well approximated as

$$\psi(\mathbf{x}, t) \approx \psi_2(\mathbf{x}_\perp, t)\, \chi_0^\varepsilon(z)\, e^{-i\,\mu_0^\varepsilon\, t}, \qquad \mathbf{x} \in \mathbb{R}^3, \quad t \geq 0. \tag{2.9}$$

Plugging (2.9) into (1.1) and then multiplying by $\chi_0^\varepsilon(z)\, e^{i\,\mu_0^\varepsilon\, t}$, integrating for z over $\mathbb{R}$, and noticing (1.2), formally we obtain

$$i\partial_t \psi_2(\mathbf{x}_\perp, t) = \left[-\frac{1}{2}\Delta_\perp + V_2(\mathbf{x}_\perp) + \frac{\kappa}{2}\,\varphi_2^\varepsilon(\mathbf{x}_\perp, t)\right]\psi_2, \qquad \mathbf{x}_\perp \in \mathbb{R}^2, \quad t > 0, \tag{2.10}$$

where

$$\begin{aligned}
\varphi_2^\varepsilon(\mathbf{x}_\perp, t) &= \int_{-\infty}^{\infty} |\chi_0^\varepsilon(z)|^2 \left[\frac{1}{2\pi|\mathbf{x}|} * (|\psi_2\chi_0^\varepsilon|^2)\right] \mathrm{d}z \\
&= \int_{\mathbb{R}^2} \left[\int_{\mathbb{R}^2} \frac{\chi_0^\varepsilon(z)^2\, \chi_0^\varepsilon(z')^2}{2\pi\sqrt{|\mathbf{x}_\perp - \mathbf{x}'_\perp|^2 + (z - z')^2}} \mathrm{d}z\mathrm{d}z'\right] |\psi_2(\mathbf{x}'_\perp, t)|^2 \mathrm{d}\mathbf{x}'_\perp \\
&:= (U_2^\varepsilon * |\psi_2|^2)(\mathbf{x}_\perp, t), \qquad \mathbf{x}_\perp \in \mathbb{R}^2, \quad t \geq 0,
\end{aligned} \tag{2.11}$$

with

$$\begin{aligned}
U_2^\varepsilon(\mathbf{x}_\perp) &= \frac{1}{2\pi}\int_{\mathbb{R}^2} \frac{\chi_0^\varepsilon(z)^2\, \chi_0^\varepsilon(z')^2}{\sqrt{|\mathbf{x}_\perp|^2 + (z - z')^2}} \mathrm{d}z\mathrm{d}z' = \frac{1}{2\pi}\int_{\mathbb{R}^2} \frac{\chi_0(z)^2\chi_0(z')^2}{\sqrt{|\mathbf{x}_\perp|^2 + \varepsilon^2\,(z - z')^2}} \mathrm{d}z\mathrm{d}z' \\
&= \frac{1}{4\pi}\int_{\mathbb{R}^2} \frac{\chi_0\left(\frac{u+v}{2}\right)^2 \chi_0\left(\frac{u-v}{2}\right)^2}{\sqrt{|\mathbf{x}_\perp|^2 + \varepsilon^2 u^2}} \mathrm{d}u\mathrm{d}v, \qquad \mathbf{x}_\perp \in \mathbb{R}^2.
\end{aligned} \tag{2.12}$$

In fact, (2.10) together with (2.11) is usually called the *surface adiabatic model* (SAM) [20]. In addition, multiplying (2.1) by $\chi_0^\varepsilon(z)$ and integrating for z over $\mathbb{R}$, noting (2.7), we get the initial data for the SAM (2.10)–(2.11) as

$$\psi_2(\mathbf{x}_\perp, 0) = \int_{\mathbb{R}} \psi_0(\mathbf{x}_\perp, z)\chi_0^\varepsilon(z)\, \mathrm{d}z = \sqrt{\varepsilon}\int_{\mathbb{R}} \psi_0(\mathbf{x}_\perp, \varepsilon u)\chi_0(u)\, \mathrm{d}u, \quad \mathbf{x}_\perp \in \mathbb{R}^2. \tag{2.13}$$

Letting $\varepsilon \to 0^+$ in (2.12) and (2.11), formally we get

$$U_2^\varepsilon(\mathbf{x}_\perp) \to \frac{1}{2\pi|\mathbf{x}_\perp|} := U_2(\mathbf{x}_\perp), \qquad \mathbf{x}_\perp \in \mathbb{R}^2, \tag{2.14}$$

$$\varphi_2^\varepsilon(\mathbf{x}_\perp, t) \to (U_2 * |\psi_2|^2)(\mathbf{x}_\perp, t) := \varphi_2(\mathbf{x}_\perp, t), \qquad \mathbf{x}_\perp \in \mathbb{R}^2, \quad t \geq 0. \tag{2.15}$$

This immediately suggests the following *surface density model* (SDM) in 2D:

$$i\partial_t\psi_2(\mathbf{x}_\perp,t)=\left[-\frac{1}{2}\Delta_\perp+V_2(\mathbf{x}_\perp)+\frac{\kappa}{2}\,\varphi_2(\mathbf{x}_\perp,t)\right]\psi_2,\qquad \mathbf{x}_\perp\in\mathbb{R}^2,\quad t>0. \tag{2.16}$$

In fact, the effective potential φ_2 in (2.15) also satisfies a fractional differential equation, namely, the "square root of Laplacian" equation [21, 33]:

$$(-\Delta_\perp)^{1/2}\varphi_2(\mathbf{x}_\perp,t)=\ |\psi_2(\mathbf{x}_\perp,t)|^2,\ \mathbf{x}_\perp\in\mathbb{R}^2,\quad \lim_{|\mathbf{x}_\perp|\to\infty}\varphi_2(\mathbf{x}_\perp,t)=0,\ t\geq 0. \tag{2.17}$$

Specifically, if the confinement in the z-direction is chosen as a harmonic oscillator potential, e.g.,

$$V_z(z)=\frac{z^2}{2},\qquad z\in\mathbb{R},$$

then we have

$$\mu_0=\frac{1}{2},\qquad \chi_0(z)=\frac{1}{\pi^{1/4}}e^{-\frac{z^2}{2}},\quad z\in\mathbb{R}. \tag{2.18}$$

Plugging (2.18) into (2.12), we obtain [22]

$$\begin{aligned}U_2^\varepsilon(\mathbf{x}_\perp)&=\frac{1}{4\pi^2}\int_{\mathbb{R}^2}\frac{e^{-\frac{u^2+v^2}{2}}}{\sqrt{|\mathbf{x}_\perp|^2+\varepsilon^2u^2}}\mathrm{d}u\mathrm{d}v=\frac{1}{(2\pi)^{3/2}}\int_{\mathbb{R}}\frac{e^{-\frac{u^2}{2}}}{\sqrt{|\mathbf{x}_\perp|^2+\varepsilon^2u^2}}\,\mathrm{d}u\\ &=\frac{2}{(2\pi)^{3/2}}\int_0^\infty\frac{e^{-\frac{u^2}{2}}}{\sqrt{|\mathbf{x}_\perp|^2+\varepsilon^2u^2}}\,\mathrm{d}u,\qquad \mathbf{x}_\perp\in\mathbb{R}^2.\end{aligned} \tag{2.19}$$

Taking the Fourier transform in (2.19), we get [22]

$$\widehat{U}_2^\varepsilon(\xi)=\frac{1}{2\pi^2}\int_{\mathbb{R}}\frac{e^{-\frac{\varepsilon^2s^2}{2}}}{|\xi|^2+s^2}\mathrm{d}s=\frac{\varepsilon}{\pi^2}\int_0^\infty\frac{e^{-\frac{s^2}{2}}}{\varepsilon^2|\xi|^2+s^2}\mathrm{d}s,\qquad \xi\in\mathbb{R}^2. \tag{2.20}$$

From (2.19) and (2.20), asymptotically, for any fixed $\varepsilon>0$, we have [22]

$$U_2^\varepsilon(\mathbf{x}_\perp)\approx\begin{cases}\frac{1}{\pi^{3/2}\sqrt{2}\,\varepsilon}\left[\ln|\mathbf{x}_\perp|+\ln(2\varepsilon)+C\right], & |\mathbf{x}_\perp|\to 0,\\ \frac{1}{2\pi|\mathbf{x}_\perp|}, & |\mathbf{x}_\perp|\to\infty,\end{cases}\qquad \mathbf{x}_\perp\in\mathbb{R}^2, \tag{2.21}$$

$$\widehat{U}_2^\varepsilon(\xi)\approx\begin{cases}\frac{1}{2\pi|\xi|}, & |\xi|\to 0,\\ \frac{1}{\sqrt{2\pi^3}\,\varepsilon}\frac{1}{|\xi|^2}, & |\xi|\to\infty,\end{cases}\qquad \xi\in\mathbb{R}^2, \tag{2.22}$$

where C is a constant. In addition, when $\varepsilon\to 0^+$ in (2.19) and (2.20), formally we get

$$U_2^\varepsilon(\mathbf{x}_\perp)\to\frac{1}{2\pi|\mathbf{x}_\perp|},\qquad \widehat{U}_2^\varepsilon(\xi)\to\frac{1}{2\pi|\xi|},\qquad \mathbf{x}_\perp,\xi\in\mathbb{R}^2. \tag{2.23}$$

2.2. From 3D to 1D. When the potential $V(\mathbf{x})$ in (1.1) is chosen as Case II (1.7), then the linear operator H can be split as

$$H=-\frac{1}{2}\Delta_\perp+\frac{1}{\varepsilon^2}V_\perp\left(\frac{\mathbf{x}_\perp}{\varepsilon}\right)-\frac{1}{2}\partial_{zz}+V_1(z):=H_\perp^\varepsilon+H_z=\frac{1}{\varepsilon^2}H_\perp^{\sim}+H_z, \tag{2.24}$$

where $\Delta_\perp = \partial_{xx} + \partial_{yy}$, $\mathbf{x}_\perp = \varepsilon\, \widetilde{\mathbf{x}}_\perp$, $\Delta_{\widetilde{\perp}} = \partial_{\tilde{x}\tilde{x}} + \partial_{\tilde{y}\tilde{y}}$, and

$$H_\perp^\varepsilon := -\frac{1}{2}\Delta_\perp + \frac{1}{\varepsilon^2} V_\perp\left(\frac{\mathbf{x}_\perp}{\varepsilon}\right) = \frac{1}{\varepsilon^2}\left[-\frac{1}{2}\Delta_{\widetilde{\perp}} + V_\perp(\widetilde{\mathbf{x}}_\perp)\right] := \frac{1}{\varepsilon^2} H_{\widetilde{\perp}}, \tag{2.25}$$

$$H_{\widetilde{\perp}} = -\frac{1}{2}\Delta_{\widetilde{\perp}} + V_\perp\left(\widetilde{\mathbf{x}}_\perp\right), \qquad H_z := -\frac{1}{2}\partial_{zz} + V_1\left(z\right). \tag{2.26}$$

For $H_{\widetilde{\perp}}$ in (2.26), due to (1.7), we know that the following eigenvalue problem admits distinct orthonormal eigenfunctions:

$$H_{\widetilde{\perp}}\zeta(\widetilde{\mathbf{x}}_\perp) = \left[-\frac{1}{2}\Delta_{\widetilde{\perp}} + V_\perp\left(\widetilde{\mathbf{x}}_\perp\right)\right]\zeta(\widetilde{\mathbf{x}}_\perp) = \lambda\zeta(\widetilde{\mathbf{x}}_\perp), \qquad \widetilde{\mathbf{x}}_\perp \in \mathbb{R}^2, \tag{2.27}$$

with $\|\zeta\|^2 := \int_{\mathbb{R}^2} |\zeta(\widetilde{\mathbf{x}}_\perp)|^2 d\widetilde{\mathbf{x}}_\perp = 1$. In fact, they can be chosen to form an orthogonal basis of $L^2(\mathbb{R}^2)$ and be denoted by $\{\zeta_k(\widetilde{\mathbf{x}}_\perp)\}$ with corresponding eigenvalues $\{\lambda_k\}$ satisfying $\lambda_0 < \lambda_1 \le \lambda_2 \le \cdots$. Thus $(\zeta_k^\varepsilon, \lambda_k^\varepsilon)$ with

$$\lambda_k^\varepsilon = \frac{\lambda_k}{\varepsilon^2}, \qquad \zeta_k^\varepsilon(\mathbf{x}_\perp) = \frac{1}{\varepsilon}\zeta_k\left(\frac{\widetilde{\mathbf{x}}_\perp}{\varepsilon}\right), \qquad k = 0, 1, 2, \ldots,$$

are orthonormal eigenpairs to the operator $H_\perp^\varepsilon$.

Again, here we only consider the "pure state" case in the strong confinement direction, especially the "ground state" case [19, 20]. Similarly, we assume that the initial data ψ_0 in (2.1) satisfies

$$\psi_0(\mathbf{x}) \approx \psi_1(z)\zeta_0^\varepsilon(\mathbf{x}_\perp), \qquad \mathbf{x} \in \mathbb{R}^3, \qquad 0 < \varepsilon \ll 1; \tag{2.28}$$

noting the scale separation in (2.24), when $\varepsilon \to 0^+$, the solution ψ to the 3D SPS (1.1)–(1.2) can be approximated as

$$\psi(\mathbf{x}, t) \approx \psi_1(z, t)\, \zeta_0^\varepsilon(\mathbf{x}_\perp)\, e^{-i\,\lambda_0^\varepsilon\, t}, \qquad \mathbf{x} \in \mathbb{R}^3, \quad t \ge 0. \tag{2.29}$$

Plugging (2.29) into (1.1) and then multiplying by $\zeta_0^\varepsilon(\mathbf{x}_\perp)\, e^{i\,\lambda_0^\varepsilon\, t}$, integrating for $\mathbf{x}_\perp$ over $\mathbb{R}^2$, and noticing (1.2), formally we obtain

$$i\partial_t\psi_1(z, t) = \left[-\frac{1}{2}\partial_{zz} + V_1(z) + \frac{\kappa}{2\pi}\,\varphi_1^\varepsilon(z, t)\right]\psi_1, \qquad z \in \mathbb{R}, \quad t > 0, \tag{2.30}$$

where

$$\begin{aligned}
\varphi_1^\varepsilon(z, t) &= \int_{\mathrm{R}^2} |\zeta_0^\varepsilon(\mathbf{x}_\perp)|^2 \left[\frac{1}{2|\mathbf{x}|} * (|\psi_1\zeta_0^\varepsilon|^2)\right] \mathrm{d}\mathbf{x}_\perp \\
&= \int_{\mathbb{R}} \left[\int_{\mathbb{R}^2}\int_{\mathbb{R}^2} \frac{\zeta_0^\varepsilon(\mathbf{x}_\perp)^2\, \zeta_0^\varepsilon(\mathbf{x}'_\perp)^2}{2\sqrt{|\mathbf{x}_\perp - \mathbf{x}'_\perp|^2 + (z - z')^2}} \mathrm{d}\mathbf{x}_\perp \mathrm{d}\mathbf{x}'_\perp\right] |\psi_1(z', t)|^2 \mathrm{d}z' \\
&:= (U_1^\varepsilon * |\psi_1|^2)(z, t), \qquad z \in \mathbb{R}, \quad t \ge 0,
\end{aligned} \tag{2.31}$$

with

$$\begin{aligned}
U_1^\varepsilon(z) &= \frac{1}{2}\int_{\mathbb{R}^2}\int_{\mathbb{R}^2} \frac{\zeta_0^\varepsilon(\mathbf{x}_\perp)^2\, \zeta_0^\varepsilon(\mathbf{x}'_\perp)^2}{\sqrt{|z|^2 + |\mathbf{x}_\perp - \mathbf{x}'_\perp|^2}} \mathrm{d}\mathbf{x}_\perp \mathrm{d}\mathbf{x}'_\perp \\
&= \frac{1}{2}\int_{\mathbb{R}^2}\int_{\mathbb{R}^2} \frac{\zeta_0(\mathbf{x}_\perp)^2 \zeta_0(\mathbf{x}'_\perp)^2}{\sqrt{|z|^2 + \varepsilon^2|\mathbf{x}_\perp - \mathbf{x}'_\perp|^2}} \mathrm{d}\mathbf{x}_\perp \mathrm{d}\mathbf{x}'_\perp \\
&= \frac{1}{8}\int_{\mathbb{R}^2}\int_{\mathbb{R}^2} \frac{\zeta_0\left(\frac{\mathbf{u}+\mathbf{v}}{2}\right)^2 \zeta_0\left(\frac{\mathbf{u}-\mathbf{v}}{2}\right)^2}{\sqrt{|z|^2 + \varepsilon^2|\mathbf{u}|^2}} \mathrm{d}\mathbf{u}\mathrm{d}\mathbf{v}, \qquad z \in \mathbb{R}.
\end{aligned} \tag{2.32}$$

Equation (2.30) together with (2.31) is named as *line adiabatic model* (LAM). In addition, multiplying (2.1) by $\zeta_0^\varepsilon(\mathbf{x}_\perp)$ and integrating for $\mathbf{x}_\perp$ over $\mathbb{R}^2$, we get the initial data for LAM as

$$\psi_1(z,0)=\int_{\mathbb{R}^2}\psi_0(\mathbf{x}_\perp,z)\,\zeta_0^\varepsilon(\mathbf{x}_\perp)\,\mathrm{d}\mathbf{x}_\perp=\varepsilon\int_{\mathbb{R}^2}\psi_0(\varepsilon\mathbf{u},z)\,\zeta_0(\mathbf{u})\,\mathrm{d}\mathbf{u},\quad z\in\mathbb{R}. \tag{2.33}$$

Again, if letting $\varepsilon\to 0^+$ in (2.32), formally we get

$$U_1^\varepsilon(z)\to\frac{1}{2|z|}:=U_1(z),\qquad z\in\mathbb{R}. \tag{2.34}$$

In fact, $U_1(z)$ is too singular at $z=0$ to be a kernel in 1D. The mathematical difficulty of defining the convolution with the correct interaction potential for point particles in 1D is an indication that the contradiction between Heisenberg's uncertainty principle and the complete confinement is even more pronounced in 1D than in 2D.

Specifically, if the confinement in the $\mathbf{x}_\perp$-plane is chosen as a harmonic oscillator potential, e.g.,

$$V_\perp(\mathbf{x}_\perp)=\frac{1}{2}\left(x^2+y^2\right),\qquad \mathbf{x}_\perp=(x,y)\in\mathbb{R}^2,$$

then we have

$$\lambda_0=1,\qquad \zeta_0(\mathbf{x}_\perp)=\frac{1}{\sqrt{\pi}}e^{-\frac{x^2+y^2}{2}}. \tag{2.35}$$

Plugging (2.35) into (2.32), we obtain

$$\begin{aligned}U_1^\varepsilon(z)&=\frac{1}{8\pi^2}\int_{\mathbb{R}^2}\int_{\mathbb{R}^2}\frac{e^{-\frac{|\mathbf{u}|^2}{2}}e^{-\frac{|\mathbf{v}|^2}{2}}}{\sqrt{|z|^2+\varepsilon^2|\mathbf{u}|^2}}\mathrm{d}\mathbf{u}\mathrm{d}\mathbf{v}=\frac{1}{4\pi}\int_{\mathbb{R}^2}\frac{e^{-\frac{|\mathbf{u}|^2}{2}}}{\sqrt{|z|^2+\varepsilon^2|\mathbf{u}|^2}}\mathrm{d}\mathbf{u}\\ &=\frac{1}{4}\int_0^\infty\frac{e^{-\frac{u}{2}}}{\sqrt{z^2+\varepsilon^2u}}\,\mathrm{d}u=\frac{1}{4\varepsilon^2}\int_0^\infty\frac{e^{-\frac{u}{2\varepsilon^2}}}{\sqrt{z^2+u}}\,\mathrm{d}u,\qquad z\in\mathbb{R}.\end{aligned} \tag{2.36}$$

Taking the Fourier transform in (2.36), we get [22]

$$\widehat{U}_1^\varepsilon(\xi)=\frac{1}{2\sqrt{2\pi}}\int_0^\infty\frac{e^{-\frac{\varepsilon^2 s}{2}}}{|\xi|^2+s}\mathrm{d}s=\frac{1}{2\sqrt{2\pi}}\int_0^\infty\frac{e^{-\frac{s}{2}}}{\varepsilon^2|\xi|^2+s}\mathrm{d}s,\qquad \xi\in\mathbb{R}. \tag{2.37}$$

From (2.36) and (2.37), asymptotically, for any fixed $\varepsilon>0$, we have [22]

$$U_1^\varepsilon(z)\approx\begin{cases}\frac{\sqrt{2\pi}}{4}\left(\frac{1}{\varepsilon}-\sqrt{\frac{2}{\pi}}\frac{1}{\varepsilon^2}|z|\right), & |z|\to 0,\\ \frac{1}{2|z|}, & |z|\to\infty,\end{cases}\qquad z\in\mathbb{R}, \tag{2.38}$$

$$\widehat{U}_1^\varepsilon(\xi)\approx\begin{cases}\frac{1}{2\sqrt{2\pi}}\left[\ln 2-\gamma_e-2\ln(\varepsilon|\xi|)\right], & |\xi|\to 0,\\ \frac{1}{\sqrt{2\pi}\,\varepsilon^2|\xi|^2}, & |\xi|\to\infty,\end{cases}\qquad \xi\in\mathbb{R}, \tag{2.39}$$

where γ_e is the Euler–Mascheroni constant. In addition, when $\varepsilon\to 0^+$ in (2.36) and (2.37), formally we get

$$U_1^\varepsilon(z)\to\frac{1}{2|z|},\qquad \widehat{U}_1^\varepsilon(\xi)\to\infty,\qquad z,\xi\in\mathbb{R}. \tag{2.40}$$

2.3. Models in a unified formulation. The 2D SAM (2.10)–(2.11) with (2.19) (or (2.12)) and SDM (2.16)–(2.17) and 1D LAM (2.30)–(2.31) with (2.36) (or (2.32)) can be written in a unified formulation as a *general nonlinear Schrödinger equation* (GNLS), which is the same as the SPS (1.3)–(1.4) with different interaction kernels in different cases:

$$i\,\partial_t\psi(\mathbf{x},t) = \left[-\frac{1}{2}\Delta + V(\mathbf{x}) + \beta\,\varphi\right]\,\psi, \qquad \mathbf{x}\in\mathbb{R}^d, \quad t>0, \tag{2.41}$$

$$\varphi(\mathbf{x},t) = U_d * |\psi|^2, \qquad \mathbf{x}\in\mathbb{R}^d, \quad t\geq 0, \tag{2.42}$$

where $\mathbf{x}=(x,y)$ and $\beta=\frac{\kappa}{2}$ if $d=2$, and $\mathbf{x}=x$ and $\beta=\frac{\kappa}{2\pi}$ if $d=1$, and

$$U_d(\mathbf{x}) = \begin{cases} U_2^\varepsilon(\mathbf{x}), \\ \frac{1}{2\pi|\mathbf{x}|}, \\ U_1^\varepsilon(\mathbf{x}), \end{cases} \Leftrightarrow \widehat{U}_d(\xi) = \begin{cases} \frac{\varepsilon}{\pi^2}\int_0^\infty \frac{e^{-s^2/2}}{\varepsilon^2|\xi|^2+s^2}\mathrm{d}s, & d=2 \text{ and SAM}, \\ \frac{1}{2\pi|\xi|}, & d=2 \text{ and SDM}, \\ \frac{1}{2\sqrt{2\pi}}\int_0^\infty \frac{e^{-s/2}}{\varepsilon^2|\xi|^2+s}\mathrm{d}s, & d=1 \text{ and LAM}. \end{cases} \tag{2.43}$$

For studying the dynamics of GLSE, the following initial condition is usually given:

$$\psi(\mathbf{x},0) = \psi_0(\mathbf{x}), \quad \mathbf{x}\in\mathbb{R}^d. \tag{2.44}$$

2.4. Conservation laws and ground states. Two important conserved quantities for the GNLS (2.41)–(2.42) are the *mass* or *normalization*,

$$N(t) := N(\psi(\cdot,t)) = \int_{\mathbb{R}^d} |\psi(\mathbf{x},t)|^2\,\mathrm{d}\mathbf{x} \equiv \int_{\mathbb{R}^d} |\psi_0(\mathbf{x})|^2\,\mathrm{d}\mathbf{x}, \quad t\geq 0, \tag{2.45}$$

and the *energy*,

$$\begin{aligned} E(t) := E(\psi(\cdot,t)) &= \int_{\mathbb{R}^d}\left[\frac{1}{2}|\nabla\psi(\mathbf{x},t)|^2 + \left(V(\mathbf{x}) + \frac{\beta}{2}(U_d*|\psi|^2)\right)|\psi(\mathbf{x},t)|^2\right]\mathrm{d}\mathbf{x} \\ &= \int_{\mathbb{R}^d}\left[\frac{1}{2}|\nabla\psi(\mathbf{x},t)|^2 + \left(V(\mathbf{x}) + \frac{\beta}{2}\varphi\right)|\psi(\mathbf{x},t)|^2\right]\mathrm{d}\mathbf{x} \equiv E(0), \quad t\geq 0. \end{aligned} \tag{2.46}$$

The ground state $\phi_g := \phi_g(\mathbf{x})$ of the GNLS (2.41)–(2.42) is usually defined as the minimizer of the energy functional over the unit sphere $S = \{\phi := \phi(\mathbf{x}) \,|\, \|\phi\|^2 = 1,\ E(\phi)<\infty\}$:

$$E^g := E(\phi_g) = \min_{\phi\in S}\ E(\phi), \tag{2.47}$$

where

$$E(\phi) = \int_{\mathbb{R}^d}\left[\frac{1}{2}|\nabla\phi(\mathbf{x})|^2 + \left(V(\mathbf{x}) + \frac{\beta}{2}\varphi(\mathbf{x})\right)|\phi(\mathbf{x})|^2\right]\mathrm{d}\mathbf{x}, \qquad \varphi(\mathbf{x}) = U_d*|\phi|^2.$$

It is easy to see that the Euler–Lagrange equation of the above nonconvex minimization problem is the following nonlinear eigenvalue problem, i.e., find $\mu\in\mathbb{R}$ and $\phi\in S$ such that

$$\mu\phi(\mathbf{x}) = \left[-\frac{1}{2}\Delta + V(\mathbf{x}) + \beta\,\varphi\right]\phi(\mathbf{x}), \qquad \varphi(\mathbf{x}) = U_d*|\phi|^2, \qquad \mathbf{x}\in\mathbb{R}^d, \tag{2.48}$$

where the eigenvalue μ (or chemical potential) can be computed as

$$\mu := \mu(\phi) = \int_{\mathbb{R}^d} \left[\frac{1}{2} |\nabla \phi(\mathbf{x})|^2 + \left(V(\mathbf{x}) + \beta \left(U_d * |\phi|^2 \right) \right) |\phi|^2 \right] \mathrm{d}\mathbf{x}$$
$$= E(\phi) + \frac{\beta}{2} \int_{\mathbb{R}^d} (U_d * |\phi|^2) \, |\phi|^2 \, \mathrm{d}\mathbf{x} = E(\phi) + \frac{\beta}{2} \int_{\mathbb{R}^d} \varphi(\mathbf{x}) |\phi(\mathbf{x})|^2 \, \mathrm{d}\mathbf{x}.$$

For existence and uniqueness of the ground state to (2.47), we refer the reader to [4, 5]; for well-posedness and dynamical properties of the SPS (1.3)–(1.4) and the GNLS (2.41)–(2.42), we refer the reader to [4, 5, 23, 38] and references therein; and for analytical and asymptotic analysis on dimension reduction from the 3D SPS to 2D SAM and SDM, we refer the reader to [19] and references therein.

3. Numerical methods. In order to verify numerically the dimension reduction from the 3D SPS (1.1)–(1.2) to the 2D SAM (2.10)–(2.11) with (2.19) and SDM (2.16)–(2.17) and 1D LAM (2.30)–(2.31) with (2.36), to find numerically the convergence rates for the dimension reduction, and to simulate numerically low-dimensional quantum systems based on the 2D and 1D models, in this section, we briefly introduce numerical methods for computing ground states and dynamics of the 2D SAM and SDM and 1D LAM as well as 2D SPS models. For efficient and accurate numerical methods for computing ground states and dynamics of the SPS (1.3)–(1.4) in 3D and 1D, we refer the reader to [26, 50] and references therein. In practical computations, the whole space problems (2.41)–(2.42) and (2.47) are usually truncated into a bounded computational domain $\Omega \subset \mathbb{R}^d$ which is usually chosen as an interval $[a, b]$ in 1D, a rectangle $[a, b] \times [c, d]$ in 2D, and a box $[a, b] \times [c, d] \times [e, f]$ in 3D. Choose a time step $\tau := \Delta t > 0$ and mesh sizes $h_x = \frac{b-a}{J}$, $h_y = \frac{d-c}{K}$, and $h_z = \frac{f-e}{L}$ with J, K, and L positive even integers, and denote time steps as $t_n = n\,\tau$ for $n = 0, 1, \ldots$, and grid points as $x_j = a + j\,h_x$ for $j = 0, 1, \ldots, J$, $y_k = c + k\,h_y$ for $k = 0, 1, \ldots, K$, and $z_l = e + l\,h_z$ for $l = 0, 1, \ldots, L$.

3.1. A method for computing ground states. For computing the ground states of (2.47), we adapt the *gradient flow with discrete normalization* (GFDN), which has been widely and successfully used for computing ground states of the Gross–Pitaevskii equation (GPE) with application to Bose–Einstein condensation (BEC) [6, 7]. From time $t = t_n$ to $t = t_{n+1}$, applying the steepest descent method to the energy functional $E(\phi)$ in (2.46) without the constraint (2.45), and then projecting the solution back to the unit sphere S at the end of each time interval $[t_n, t_{n+1}]$ to ensure the constraint (2.45), we obtain the following gradient flow for $\phi := \phi(\mathbf{x}, t)$ with discrete normalization, which is truncated on Ω as

$$\partial_t \phi(\mathbf{x}, t) = -\frac{1}{2} \frac{\delta E(\phi)}{\delta \phi} = \left[\frac{1}{2} \Delta - V(\mathbf{x}) - \beta \varphi \right] \phi, \qquad \mathbf{x} \in \Omega, \quad t_n \le t < t_{n+1}, \tag{3.1}$$

$$\varphi(\mathbf{x}, t) = U_d * \rho = \int_{\mathbb{R}^d} U_d(\mathbf{x} - \mathbf{u}) \rho(\mathbf{u}, t) \, \mathrm{d}\mathbf{u}, \qquad \mathbf{x} \in \Omega, \quad t_n \le t < t_{n+1}, \tag{3.2}$$

$$\phi(\mathbf{x}, t_{n+1}) := \phi(\mathbf{x}, t_{n+1}^+) = \frac{\phi(\mathbf{x}, t_{n+1}^-)}{\|\phi(\mathbf{x}, t_{n+1}^-)\|}, \qquad \mathbf{x} \in \Omega, \quad n \ge 0, \tag{3.3}$$

where $\phi(\mathbf{x}, t_n^\pm) := \lim_{t \to t_n^\pm} \phi(\mathbf{x}, t)$ and

$$\rho(\mathbf{x}, t) = \begin{cases} |\phi(\mathbf{x}, t)|^2, & \mathbf{x} \in \Omega, \\ 0 & \text{otherwise}, \end{cases} \qquad \mathbf{x} \in \mathbb{R}^d. \tag{3.4}$$

The initial data is given as $\phi(\mathbf{x},0)=\phi_0(\mathbf{x})$ satisfying $\|\phi_0\|^2=\int_\Omega|\phi_0(\mathbf{x})|^2d\mathbf{x}=1$. The boundary condition to (3.1) will be chosen as either the periodic boundary condition or the homogeneous Dirichlet boundary condition based on the kernel function U_d defined in (2.43) or (1.5), which will be specified clearly below. The gradient flow (3.1) with periodic boundary condition and homogeneous Dirichlet boundary condition will be discretized by the backward Euler Fourier and sine pseudospectral methods, respectively [6]. The project step (3.3) will be discretized by summation [6]. The discretization to (3.2) will be presented in details in the following subsections.

3.2. A method for computing dynamics. For computing the dynamics, we adapt the *time-splitting spectral method* (TSSP), which has been widely and successfully used for the NLS equation with many applications [10, 11]. From $t=t_n$ to $t=t_{n+1}$, the problem (2.41) will be truncated on Ω and solved in two steps. First we solve the free Schrödinger equation

$$i\,\partial_t\psi(\mathbf{x},t)=-\frac{1}{2}\Delta\psi(\mathbf{x},t),\qquad \mathbf{x}\in\Omega,\qquad t_n\le t\le t_{n+1}, \tag{3.5}$$

for a time step of length τ, and then we solve for $\mathbf{x}\in\Omega$ and $t_n\le t\le t_{n+1}$

$$i\,\partial_t\psi(\mathbf{x},t)=\left[V(\mathbf{x})+\beta\varphi(\mathbf{x},t)\right]\psi(\mathbf{x},t),\qquad \varphi(\mathbf{x},t)=U_d*\rho, \tag{3.6}$$

for the same time step with

$$\rho(\mathbf{x},t)=\begin{cases}|\psi(\mathbf{x},t)|^2, & \mathbf{x}\in\Omega,\\ 0 & \text{otherwise},\end{cases}\qquad \mathbf{x}\in\mathbb{R}^d. \tag{3.7}$$

Again, the boundary condition to (3.5) will be chosen as either periodic boundary condition or homogeneous Dirichlet boundary condition based on the kernel function U_d defined in (2.43) or (1.5), which will be specified clearly below. Then (3.5) is discretized in space by Fourier or sine pseudospectral methods and then integrated exactly in time. If the homogeneous Dirichlet boundary condition is used to (3.5), then we choose the sine pseudospectral method to discretize it; otherwise, the Fourier pseudospectral method is adapted if the periodic boundary condition is used to (3.5). For more details, we refer the reader to [5, 9, 10, 11, 46] and references therein.

On the other hand, we notice that on each time interval $[t_n,t_{n+1}]$, the problem (3.6) leaves $|\psi(\mathbf{x},t)|$ and hence $\varphi(\mathbf{x},t)$ invariant [9, 10, 11], i.e., $|\psi(\mathbf{x},t)|=|\psi(\mathbf{x},t_n)|$ and $\varphi(\mathbf{x},t)=\varphi(\mathbf{x},t_n)$ for all times $t_n\le t\le t_{n+1}$. Thus, for $t\in[t_n,t_{n+1}]$, (3.6) reduces to

$$i\,\partial_t\psi(\mathbf{x},t)=\left[V(\mathbf{x})+\beta\varphi(\mathbf{x},t_n)\right]\psi(\mathbf{x},t),\qquad \varphi(\mathbf{x},t_n)=U_d*\rho_n, \tag{3.8}$$

for $\mathbf{x}\in\Omega$ and $t_n\le t\le t_{n+1}$ with

$$\rho_n(\mathbf{x})=\begin{cases}|\psi(\mathbf{x},t_n)|^2, & \mathbf{x}\in\Omega,\\ 0 & \text{otherwise},\end{cases}\qquad \mathbf{x}\in\mathbb{R}^d. \tag{3.9}$$

Integrating the first equation in (3.8) in time gives

$$\psi(\mathbf{x},t)=\psi(\mathbf{x},t_n)\,e^{-i[V(\mathbf{x})+\beta\varphi(\mathbf{x},t_n)](t-t_n)},\quad \mathbf{x}\in\Omega,\quad t_n\le t\le t_{n+1}. \tag{3.10}$$

In the following subsections, we will discuss in detail the approximation of φ in (3.8). The approximation of φ in (3.2) can be done in a similar way, and thus we omit the details for brevity.

We note here that, in practice, we always use the second-order Strang splitting method [47] to combine the two steps in (3.5) and (3.6). That is, from time $t = t_n$ to $t = t_{n+1}$, we (i) evolve (3.5) for half time step $\tau/2$ with initial data given at $t = t_n$; (ii) evolve (3.6) for one step τ starting with the new data; and (iii) evolve (3.5) for half time step $\tau/2$ again with the newer data. For a more general discussion of the splitting method, we refer the reader to [5, 49].

3.3. Computation of $\varphi(\mathbf{x}, t_n)$ in (3.8). Due to the convolution in (3.8), it is natural to consider using the Fourier transform to compute $\varphi(\mathbf{x}, t_n)$. However, from (2.43) or (1.5) and (2.45), we know that $\lim_{\xi\to 0} \widehat{U}_d(\xi) = \infty$ and $\widehat{\rho}_n(\xi = 0) \neq 0$. As noted for simulating dipolar BECs in 3D [5], there is a numerical locking phenomena, i.e., numerical errors will be bounded below no matter how small the mesh size is, when one uses the fast Fourier transform (FFT) to evaluate $\varphi(\mathbf{x}, t_n)$ in (3.8) directly through the Fourier transform. Here we present a method to evaluate $\varphi(\mathbf{x}, t_n)$ in (3.8) through homogenizing the mean value of $\rho(\mathbf{x}, t_n) := |\psi(\mathbf{x}, t_n)|^2$, which is a constant independent of n, to zero and then using FFT to compute it.

Denote

$$G_n(\mathbf{x}) = \rho_n(\mathbf{x}) - \frac{\mathrm{I}_\Omega}{|\Omega|} C_0 \quad \Leftrightarrow \quad \rho_n(\mathbf{x}) = G_n(\mathbf{x}) + \frac{\mathrm{I}_\Omega}{|\Omega|} C_0, \quad \mathbf{x} \in \mathbb{R}^d, \tag{3.11}$$

where $C_0 := \int_\Omega |\psi(\mathbf{x}, t_n)|^2 d\mathbf{x} \equiv \int_\Omega |\psi_0(\mathbf{x})|^2 d\mathbf{x}$ for $n \geq 0$, I_Ω is the characteristic function of the domain Ω, and $|\Omega|$ is the length/area/volume of Ω in 1D/2D/3D, respectively. Then it is easy to see that $\widehat{G}_n(\xi = 0) = 0$ and we have

$$\varphi(\mathbf{x}, t_n) = U_d * \rho_n = U_d * G_n + C_0 U_d * \frac{\mathrm{I}_\Omega}{|\Omega|} := P(\mathbf{x}, t_n) + C_0 Q(\mathbf{x}), \quad \mathbf{x} \in \Omega, \tag{3.12}$$

where $P(\mathbf{x}, t_n)$ can be evaluated via FFT and $Q(\mathbf{x})$ can be evaluated analytically. Here we only show how to compute them in 1D; extensions to 2D and 3D are straightforward and we omit them here for brevity. When $d = 1$, we have

$$Q(x) := U_1 * \frac{\mathrm{I}_\Omega}{|\Omega|} = \int_{\mathbb{R}} U_1(x-u) \frac{\mathrm{I}_\Omega}{|\Omega|} \mathrm{d}u = \frac{1}{b-a} \int_a^b U_1(x-u) \mathrm{d}u, \quad a \leq x \leq b. \tag{3.13}$$

The above definite integral can be computed either analytically, or otherwise numerically via numerical quadrature, e.g., composite Gauss quadratures or Simpson's rule. To approximate $P(x, t_n)$, we make the (approximate) ansatz

$$P(x, t_n) = \sum_{p=-J/2}^{J/2-1} \widehat{P}_p^f \, e^{i\mu_p(x-a)}, \qquad a \leq x \leq b, \tag{3.14}$$

where $\mu_p = \frac{2p\pi}{b-a}$ for $p = -\frac{J}{2}, \ldots, \frac{J}{2} - 1$, and $\widehat{P}_p^f$ is the Fourier coefficient of $P(x, t_n)$ corresponding to the frequency p. We then approximate the convolution in $P(x, t_n)$ by a discrete convolution and take its discrete Fourier transform to obtain

$$\widehat{P}_p^f = \sqrt{2\pi}\, \widehat{U}_1(\mu_p) \cdot (\widehat{|\psi^n|^2})_p^f, \qquad p = -\frac{J}{2}, \ldots, \frac{J}{2} - 1, \tag{3.15}$$

where $(\widehat{|\psi^n|^2})_p^f$ is the Fourier coefficient (through discrete Fourier transform) corresponding to the frequency p of the function $|\psi(\mathbf{x}, t_n)|^2$ defined on the grid points

of Ω and $\widehat{U}_1(\mu_p)$ is given in (2.43) or (1.5), which can be evaluated analytically or numerically via numerical quadratures. If $\varphi(\mathbf{x}, t_n)$ is approximated this way, we usually use periodic boundary conditions to (3.5) and (3.1) and discretize them by the time-splitting Fourier pseudospectral (TSFP) method [5] and backward Euler Fourier pseudospectral (BEFP) method [5, 6], respectively.

3.4. Another way to compute $\varphi(\mathbf{x}, t_n)$ in 2D SDM. For 2D SDM, the function $\varphi(\mathbf{x}, t_n)$ in (3.8) also satisfies the square-root Poisson equation in (2.17) which can be truncated on the computational domain Ω with homogeneous Dirichlet boundary conditions as

$$(-\nabla^2)^{1/2}\varphi(\mathbf{x}, t_n) = |\psi(\mathbf{x}, t_n)|^2, \quad \mathbf{x} \in \Omega; \qquad \varphi(\mathbf{x}, t_n)|_{\partial\Omega} = 0. \tag{3.16}$$

Based on this differential formulation, another way to compute $\varphi(\mathbf{x}, t_n)$ is to discretize the above problem by using a sine pseudospectral method in which the 0-mode is avoided in numerical discretization.

Denote the index set $\mathcal{T}_{JK} = \{(p, q) \,|\, 1 \le p \le J-1, 1 \le q \le K-1\}$ and assume

$$\varphi(\mathbf{x}, t_n) = \sum_{p=1}^{J-1}\sum_{q=1}^{K-1} \widehat{\varphi}^s_{pq}\, \sin(\mu^1_p(x-a))\sin(\mu^2_q(y-c)), \qquad \mathbf{x} \in \Omega, \tag{3.17}$$

where $\widehat{\varphi}^s_{pq}$ is the sine transform of $\varphi(\mathbf{x}, t_n)$ at frequency (p, q) and

$$\mu^1_p = \frac{p\pi}{b-a}, \qquad \mu^2_q = \frac{q\pi}{d-c}, \qquad (p, q) \in \mathcal{T}_{JK}. \tag{3.18}$$

Substituting (3.17) into (3.16) and taking sine transform on both sides, we obtain

$$\widehat{\varphi}^s_{pq} = \frac{(\widehat{|\psi^n|^2})^s_{pq}}{\left[(\mu^1_p)^2 + (\mu^2_q)^2\right]^{1/2}}, \qquad (p, q) \in \mathcal{T}_{JK}, \tag{3.19}$$

where $(\widehat{|\psi^n|^2})^s_{pq}$ is the sine transform coefficient (through discrete sine transform) corresponding to the frequency (p, q) of the function $|\psi(\mathbf{x}, t_n)|^2$ defined on the grid points of Ω. If $\varphi(\mathbf{x}, t_n)$ is approximated in this way, we usually use homogeneous Dirichlet boundary condition to (3.5) and (3.1) and discretize them by the time-splitting sine pseudospectral (TSSP) method [5] and backward Euler sine pseudospectral (BESP) method [9, 10, 11, 12], respectively.

Remark 3.1. For general confining potentials V_z in (1.6) and $V_\perp$ in (1.7) other than harmonic potential, one might not find explicit solutions of the first eigenfunction to the eigenvalue problems (2.6) and (2.27). In this situation, one can solve the eigenvalue problems numerically and obtain numerically the first eigenfunctions $\chi_0(\tilde{z})$ and $\zeta_0(\tilde{\mathbf{x}}_\perp)$ to (2.6) and (2.27), respectively. Then the remaining dimension reduction and numerical methods can be carried out similarly.

4. Numerical results. In this section, we report numerical results on convergence rates of the dimension reduction from 3D SPS to 2D SAM and SDM and 1D LAM; comparison between different models such as SPS, SAM, and SDM in 2D and SPS and LAM in 1D; and ground states and dynamics of 2D SAM and SDM and 1D LAM under different parameters by using the efficient and accurate numerical methods presented in the previous section. Denote by $\phi_g := \phi_g(x, y, z)$ and $\psi := \psi(x, y, z, t)$ the ground state and the solution of the dynamics at time t, respectively, of the 3D SPS (1.1)–(1.2), which are computed numerically on a computational domain $\Omega = [-8, 8]^3$. In all computations, the time step is taken as $\tau = 0.01$ for computing ground states and $\tau = 0.0001$ for computing dynamics.

TABLE 4.1
Convergence from 3D SPS to 2D SAM on ground states in terms of $\|\phi_g - \phi_g^{(2)}\chi_0^\varepsilon(z)\|_{l^2}$ *in section* 4.1*, while cubic convergence was obtained analytically in* [39].

ε	1	1/2	1/4	1/8	1/16	1/32
$\kappa = 5$	1.81E-02	3.80E-03	8.16E-04	8.81E-05	1.21E-05	1.64E-06
rate	—	2.25	2.22	3.21	2.86	2.88
$\kappa = -5$	2.01E-02	4.24E-03	9.98E-04	1.11E-04	1.57E-05	2.17E-06
rate	—	2.25	2.09	3.17	2.82	2.86

TABLE 4.2
Convergence from 3D SPS to 2D SAM on ground states in terms of $\|\chi^{(p)} - \chi_0^\varepsilon\|_{l^2}$ *in section* 4.1*, while cubic convergence was obtained analytically in* [39].

ε	1	1/2	1/4	1/8	1/16	1/32
$\kappa = 5$	1.79E-02	3.53E-03	5.71E-04	7.85E-05	1.06E-05	1.35E-06
rate	—	2.34	2.63	2.86	2.89	2.97
$\kappa = -5$	1.99E-02	3.94E-03	6.78E-04	9.88E-05	1.37E-05	1.81E-06
rate	—	2.34	2.54	2.78	2.85	2.92

TABLE 4.3
Convergence from 3D SPS to 2D SDM (top) and SPS (bottom) on ground states in terms of $\|\phi_g^{(p)} - \phi_g^{(2)}\|_{l^2}$ *in section* 4.1.

ε	1/2	1/4	1/8	1/16	1/32
$\kappa = 5$	2.39E-02	1.45E-02	7.85E-03	4.23E-03	2.25E-03
rate	—	0.72	0.89	0.89	0.91
$\kappa = -5$	2.76E-02	1.75E-02	1.05E-02	5.74E-03	3.06E-03
rate	—	0.66	0.74	0.87	0.91
$\kappa = 5$	6.49E-02	5.57E-02	4.91E-02	4.56E-02	4.37E-02
$\kappa = -5$	5.86E-02	4.85E-02	4.16E-02	3.70E-02	3.43E-02

4.1. Convergence rates from 3D SPS to 2D SAM and SDM. In order to do so, we take the external potential in (1.6) for the 3D SPS (1.1)–(1.2) as

$$V_z(z) = \frac{z^2}{2}, \qquad V_2(x,y) = \frac{1}{2}\left(x^2+y^2\right), \qquad V(x,y,z) = \frac{1}{2}\left(x^2+y^2+\frac{z^2}{\varepsilon^4}\right).$$

Let $\phi_g^{(2)} := \phi_g^{(2)}(x,y)$ be the ground state of the 2D SAM or SDM and let $\psi_2 := \psi_2(x,y,t)$ be the solution of the dynamics of the 2D SAM or SDM with initial data $\psi_0(x,y) = e^{-\frac{x^2+y^2}{2}}$ in (2.44) at time t, which are computed numerically on a computational domain $\Omega = [-16,16]^2$ with mesh sizes $h_x = h_y = 1/16$. Based on this, the initial data ψ_0 in (2.1) for 3D SPS is chosen as $\psi_0(x,y,z) = \frac{1}{\pi^{1/4}\sqrt{\varepsilon}} e^{-\frac{x^2+y^2}{2}} e^{-\frac{z^2}{2\varepsilon^2}}$ and the 3D SPS is solved with mesh sizes $h_x = h_y = \frac{1}{8}$ and $h_z = \frac{1}{128}$. Define $\phi_g^{(p)}(x,y) = \left[\int_{\mathbb{R}} |\phi_g(x,y,z)|^2 \mathrm{d}z\right]^{1/2}$, $\rho^{(p)}(x,y,t) = \int_{\mathbb{R}} |\psi(x,y,z,t)|^2 \mathrm{d}z$, and $\chi^{(p)}(z) = \left[\int_{\mathbb{R}} |\phi_g(x,y,z)|^2 \mathrm{d}x\mathrm{d}y\right]^{1/2}$ as the projections of ϕ_g and ρ over the (x,y)-plane and ϕ_g over the z-axis, respectively. Similarly, define $\rho^{(p)}(\cdot,t) = \int_{\mathbb{R}} |\psi(x,y,z,t)|^2 \mathrm{d}z$ and $\rho_2(\cdot,t) = |\psi_2(x,y,t)|^2$.

Tables 4.1 and 4.2 list errors of $\|\phi_g - \phi_g^{(2)}\chi_0^\varepsilon(z)\|_{l^2}$ and $\|\chi^{(p)} - \chi_0^\varepsilon\|_{l^2}$, respectively, which demonstrates convergence rates from 3D SPS to 2D SAM in terms of ground states with $\kappa = \pm 5$ for different ε, and Table 4.3 shows errors of $\|\phi_g^{(p)} - \phi_g^{(2)}\|_{l^2}$, which demonstrates convergence rates from 3D SPS to 2D SDM and SPS in terms

TABLE 4.4
Convergence from 3D SPS to 2D SAM on dynamics in terms of $\|\rho^{(p)} - \rho_2\|_{l^1}$ *at* $t = 1$ *in section* 4.1.

ε	1	1/2	1/4	1/8
$\kappa = 5$	1.34E-02	5.67E-03	6.91E-04	8.92E-05
rate	—	1.48	3.07	2.98
$\kappa = -5$	2.07E-02	8.19E-03	1.44E-03	1.39E-04
rate	—	1.38	2.37	3.25

TABLE 4.5
Convergence from 3D SPS to 2D SDM (top) and SPS (bottom) on dynamics in terms of $\|\rho^{(p)} - \rho_2\|_{l^1}$ *at* $t = 1$ *in section* 4.1.

ε	1/4	1/8	1/16	1/32
$\kappa = 5$	2.63E-01	1.45E-01	7.60E-02	3.90E-02
rate	—	0.86	0.93	0.96
$\kappa = -5$	5.30E-01	3.17E-01	1.77E-01	9.36E-02
rate	—	0.74	0.85	0.91
$\kappa = 5$	7.12E-2	5.72E-2	1.21E-1	1.58E-1
$\kappa = -5$	1.16	9.48E-1	8.07E-1	7.24E-1

of ground states with $\kappa = \pm 5$ for different ε. In addition, Tables 4.4 and 4.5 list errors of $\|\rho^{(p)} - \rho_2\|_{l^1}$ for $t = 1$, which demonstrates convergence rates from 3D SPS to 2D SAM and SDM and SPS, respectively, in terms of dynamics with $\kappa = \pm 5$ for different ε.

From Tables 4.1–4.5 and additional results not shown here for brevity, we can draw the following conclusions: Under harmonic confinement strongly confined in the z-direction, the 3D SPS converges to 2D SAM and SDM cubically (cf. Tables 4.1, 4.2, and 4.4) and linearly (cf. Tables 4.3 and 4.5 (top)), respectively, in terms of ε on both ground states and dynamics, which agree with the analytical results in [39] when $\varepsilon \to 0$. However, the 3D SPS doesn't converge to 2D SPS when $\varepsilon \to 0$ (cf. Tables 4.3 and 4.5 (bottom)). Based on these observations, if one wants to consider the dynamics of electrons trapped in the plane through confinement, either 2D SDM or SAM is the correct model to be adapted, and the 2D SPS might not be a good physical model in this situation.

4.2. Convergence rates from 3D SPS to 1D LAM. In order to do so, we take the external potential in (1.7) for the 3D SPS (1.1)–(1.2) as

$$V_1(z) = \frac{z^2}{2}, \qquad V_\perp(x,y) = \frac{1}{2}\left(x^2 + y^2\right), \qquad V(x,y,z) = \frac{1}{2}\left(z^2 + \frac{x^2+y^2}{\varepsilon^4}\right).$$

Let $\phi_g^{(1)} := \phi_g^{(1)}(z)$ be the ground state of the 1D LAM and let $\psi_1 := \psi_1(z,t)$ be the solution of the dynamics of the 1D LAM with initial data $\psi_0(z) = e^{-\frac{z^2}{2}}$ in (2.44) at time t, which are computed numerically on a computational domain $\Omega = [-16, 16]$ with mesh size $h_z = 1/16$. Based on this, the initial data ψ_0 in (2.1) for 3D SPS is chosen as $\psi_0(x,y,z) = \frac{1}{\sqrt{\pi}\varepsilon} e^{-\frac{x^2+y^2}{2\varepsilon^2}} e^{-\frac{z^2}{2}}$ and the 3D SPS is solved with mesh sizes as $h_x = h_y = \frac{1}{32}$ and $h_z = \frac{1}{8}$. Define $\rho^{(p)}(z,t) = \int_{\mathbb{R}^2} |\psi(x,y,z,t)|^2 \mathrm{d}x\mathrm{d}y$ to be the projection of ρ over the z-axis and let $\rho_1(\cdot,t) = |\psi_1(z,t)|^2$.

Tables 4.6 and 4.7 list errors of $\|\phi_g - \phi_g^{(1)}\zeta_0^\varepsilon(x,y)\|_{l^2}$ and $\|\rho^{(p)} - \rho_1\|_{l^1}$ at $t = 1$, which demonstrates convergence rates from 3D SPS to 1D LAM in terms of ground states and dynamics, respectively, with $\kappa = \pm 5$ for different ε.

TABLE 4.6
Convergence from 3D SPS to 1D LAM on ground states in terms of $\|\phi_g - \phi_g^{(1)}\zeta_0^\varepsilon(x,y)\|_{l^2}$ *in section* 4.2.

ε	$1/\sqrt{5}$	$1/\sqrt{10}$	$1/\sqrt{20}$	$1/\sqrt{40}$
$\kappa = 5$	6.66E-03	3.49E-03	1.79E-03	8.97E-04
rate	—	1.86	1.93	1.99
$\kappa = -5$	7.36E-03	4.04E-03	2.19E-03	1.18E-03
rate	—	1.73	1.77	1.78

TABLE 4.7
Convergence from 3D SPS to 1D LAM on dynamics in terms of $\|\rho^{(p)} - \rho_1\|_{l^1}$ *at* $t = 1$ *in section* 4.2.

ε	$1/\sqrt{10}$	$1/\sqrt{20}$	$1/\sqrt{30}$	$1/\sqrt{40}$	$1/\sqrt{50}$
$\kappa = 5$	1.02E-03	5.84E-04	4.11E-04	3.27E-04	2.71E-04
rate	—	1.61	1.73	1.59	1.68
$\kappa = -5$	1.65E-03	1.08E-03	8.29E-04	6.84E-04	5.83E-04
rate	—	1.22	1.30	1.34	1.43

TABLE 4.8
Convergence from 2D SAM to SDM on ground states in terms of $\|\phi_g - \phi_g^{(2)}\|_{l^2}$ *in section* 4.3.

ε	1	1/2	1/4	1/8	1/16	1/32
$\beta = 5$	3.37E-02	2.28E-02	1.38E-02	7.66E-03	4.01E-03	2.01E-03
rate	—	0.56	0.73	0.85	0.93	1.00
$\beta = -5$	4.01E-02	2.85E-02	1.80E-02	1.04E-02	5.68E-03	2.95E-03
rate	—	0.50	0.66	0.79	0.88	0.95

From Tables 4.6 and 4.7 and additional relevant results not shown here for brevity, we can draw the following conclusions: Under harmonic confinement strongly confined in the (x, y)-plane, the 3D SPS converges to 1D LAM quadratically (cf. Table 4.6) in terms of ε on both ground states and dynamics. Rigorous mathematical justification for these observations is ongoing.

4.3. Comparison between 2D SAM, SDM, and SPS. In order to do so, we take $d = 2$ in (2.41) for the 2D SAM, SDM, and SPS with the potential chosen as $V(x, y) = \frac{1}{2}\left(x^2 + y^2\right)$, and choose the initial data in (2.44) for computing dynamics as $\psi_0(x, y) = e^{-\frac{x^2+y^2}{2}}$.

Denote now $\phi_g := \phi_g(x, y)$ and $\psi := \psi(x, y, t)$ to be the ground state and the solution of the dynamics at time t, respectively, of the 2D SAM, which are computed numerically on a computational domain $\Omega = [-16, 16]^2$ with mesh sizes $h_x = h_y = \frac{1}{16}$. Similarly, let $\phi_g^{(2)} := \phi_g^{(2)}(x, y)$ and $\psi_2 := \psi_2(x, y, t)$ be the ground state and the solution of the dynamics at time $t = 1$ of the 2D SDM or SPS, which again are computed numerically on the same domain with the same mesh sizes and time step as well as the same initial data for dynamics as for 2D SAM.

Tables 4.8 and 4.9 list errors of $\|\phi_g - \phi_g^{(2)}\|_{l^2}$ and $\||\psi|^2 - |\psi_2|^2\|_{l^1}$ at $t = 1$, which demonstrate convergence rates from 2D SAM to SDM in terms of ground states and dynamics, respectively, with $\beta = \pm 5$ for different ε. In addition, Figure 4.1 plots the right half profile of the ground state $\phi_g(x, 0)$ (due to symmetric property) of 2D SDM and SPS for different β, and Figure 4.2 compares the ground state $\phi_g(x, 0)$ and $\phi_g(0, y)$ of 2D SDM and SPS with $\beta = 50$ and potential $V = \frac{1}{2}(x^2 + 4y^2)$.

From Tables 4.8 and 4.9 and Figures 4.1 and 4.2 as well as additional results

TABLE 4.9
Convergence from 2D SAM to SDM on dynamics in terms of $\||\psi|^2 - |\psi_2|^2\|_{l^1}$ *at* $t = 1$ *in section* 4.3.

ε	1	1/2	1/4	1/8	1/16	1/32
$\beta = 5$	5.50E-01	3.67E-01	2.19E-01	1.21E-01	6.35E-02	3.25E-02
rate	—	0.58	0.75	0.86	0.92	0.97
$\beta = -5$	8.74E-01	6.36E-01	4.12E-01	2.42E-01	1.33E-01	6.99E-02
rate	—	0.46	0.63	0.77	0.87	0.93

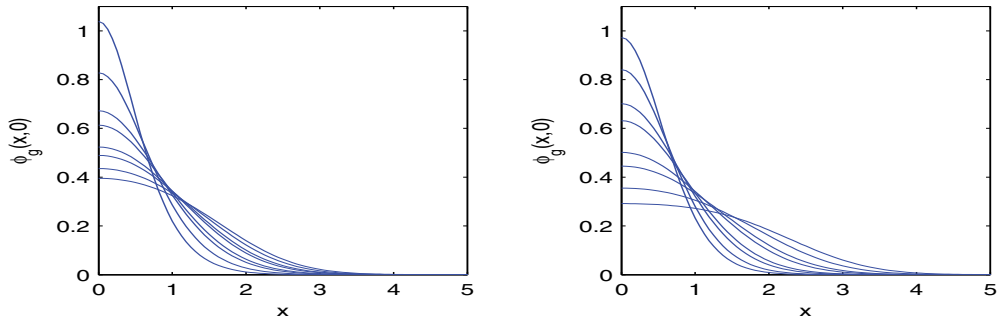

FIG. 4.1. *Plots of the ground state* $\phi_g(x, 0)$ *of 2D SDM (left) and SPS (right) for* $\beta = -30$, -20, -10, -5, 5, 10, 20, 30 *(with decreasing peaks) in section* 4.3.

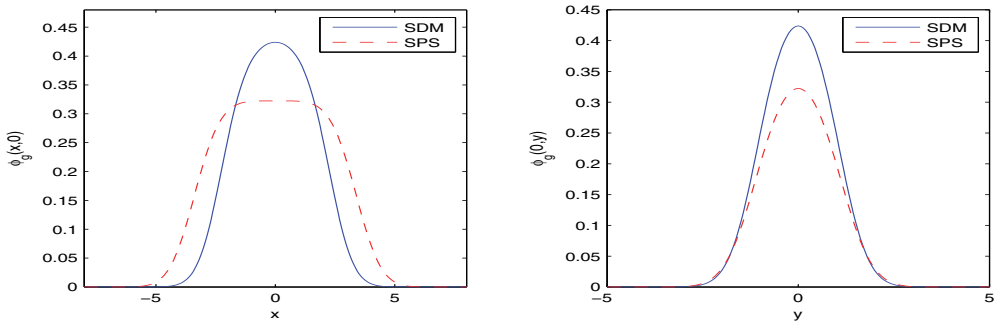

FIG. 4.2. *Plots of the ground state* $\phi_g(x, 0)$ *(left) and* $\phi_g(0, y)$ *(right) of 2D SDM (solid line) and SPS (dashed line) for* $\beta = 50$ *in section* 4.3.

not shown here for brevity, we can draw the following conclusions: When $\varepsilon \to 0$, the 2D SAM converges linearly to SDM (cf. Tables 4.8 and 4.9) on both ground states and dynamics. Again, rigorous mathematical justification for these observations is ongoing. In addition, the profiles of the ground states from 2D SDM and SPS under the same potential and interaction parameter differ significantly, especially at the center and the tail (cf. Figures 4.1 and 4.2).

4.4. Comparison between 1D LAM and SPS. In order to do so, we take $d = 1$ in (2.41) for the 1D LAM and SPS with the potential chosen as $V(x) = \frac{x^2}{2}$, and choose the initial data in (2.44) for computing dynamics as $\psi_0(x) = \frac{1}{\pi^{1/4}} e^{-\frac{x^2}{2}}$.

Denote now $\phi_g := \phi_g(x)$ and $\psi := \psi(x, t)$ to be the ground state and the solution of the dynamics at time t, respectively, of the 1D LAM or SPS, which are computed

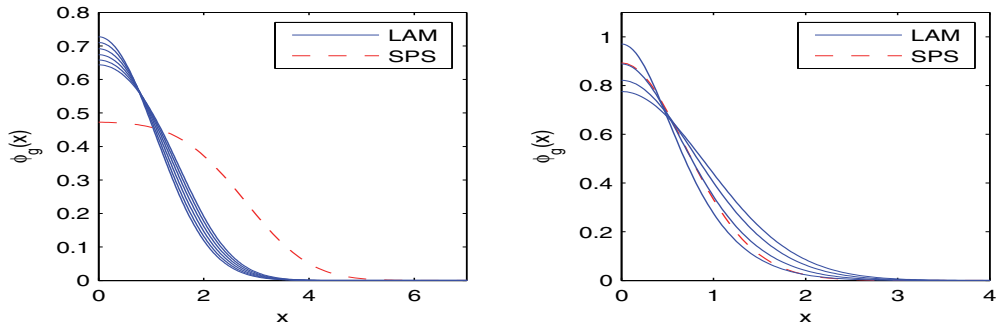

FIG. 4.3. *Plots of the ground state $\phi_g(x)$ of 1D SPS (dashed line) and LAM (solid lines) for (left) $\kappa = 5$ and $\varepsilon = 1/2,\ 1/4,\ 1/8,\ 1/16,\ 1/32$, and $1/64$ (with decreasing peaks) in LAM; (right) $\kappa = -5$ and $\varepsilon = 1/2,\ 1/8,\ 1/32$, and $1/128$ (with increasing peaks) in LAM in section* 4.4.

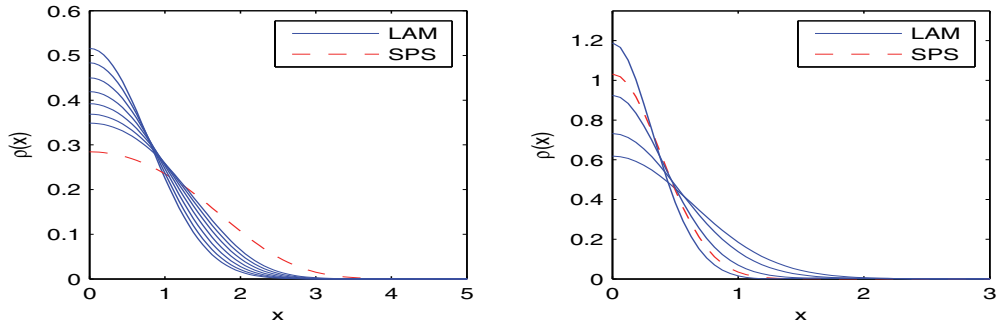

FIG. 4.4. *Plots of the density $\rho(x, t = 1)$ of the dynamics of 1D SPS (dashed line) and LAM (solid lines) for (left) $\kappa = 5$ and $\varepsilon = 1/2,\ 1/4,\ 1/8,\ 1/16,\ 1/32$, and $1/64$ (with decreasing peaks) in LAM; (right) $\kappa = -5$ and $\varepsilon = 1/2,\ 1/8,\ 1/32$, and $1/128$ (with increasing peaks) in LAM in section* 4.4.

numerically on a computational domain $\Omega = [-16, 16]$ with mesh size $h_x = \frac{1}{16}$, and define the density $\rho(x,t) := |\psi(x,t)|^2$. Figures 4.3 and 4.4 show the ground state $\phi_g(x)$ and the density $\rho(x,t)$ at $t = 1$ of the dynamics, respectively, of 1D SPS and 1D LAM with different ε.

From Figures 4.3 and 4.4 as well as additional results not shown here for brevity, we can draw the following conclusions: The profiles of the ground states and dynamics from 1D SPS and LAM under the same potential and interaction parameter differ significantly, especially at the center and the tail (cf. Figures 4.3 and 4.4).

4.5. Ground states and dynamics of electrons in 2D via SDM. Here we present some numerical results on the ground states and dynamics of electrons in 2D with application to graphene through the 2D SDM (2.16)–(2.17), which is much cheaper than solving the 3D SPS.

For computing the ground states, we take harmonic and harmonic + honeycomb [24] potentials defined as

$$V(x,y) = \frac{1}{2}(x^2 + 4\,y^2), \tag{4.1}$$

$$V(x,y) = \frac{1}{2}\left(x^2 + y^2\right) + V_0\left[\cos(\mathbf{b_1}\cdot\mathbf{x}) + \cos(\mathbf{b_2}\cdot\mathbf{x}) + \cos((\mathbf{b_1}+\mathbf{b_2})\cdot\mathbf{x})\right], \tag{4.2}$$

TABLE 4.10
Different quantities of the ground state in 2D SDM with harmonic potential (4.1) *for different* β *in section* 4.5.

β	E^g	$E^g_{\rm kin}$	$E^g_{\rm pot}$	$E^g_{\rm int}$	σ^g_x	σ^g_y	$\rho_g(\mathbf{0})$
-50	-2.989	3.554	0.181	-6.723	0.075	0.071	1.619
-10	0.874	0.942	0.604	-0.672	0.353	0.214	0.784
-5	1.198	0.834	0.676	-0.312	0.423	0.233	0.723
5	1.783	0.684	0.824	0.274	0.582	0.266	0.627
10	2.050	0.634	0.896	0.520	0.668	0.281	0.589
50	3.830	0.442	1.432	1.956	1.356	0.377	0.424

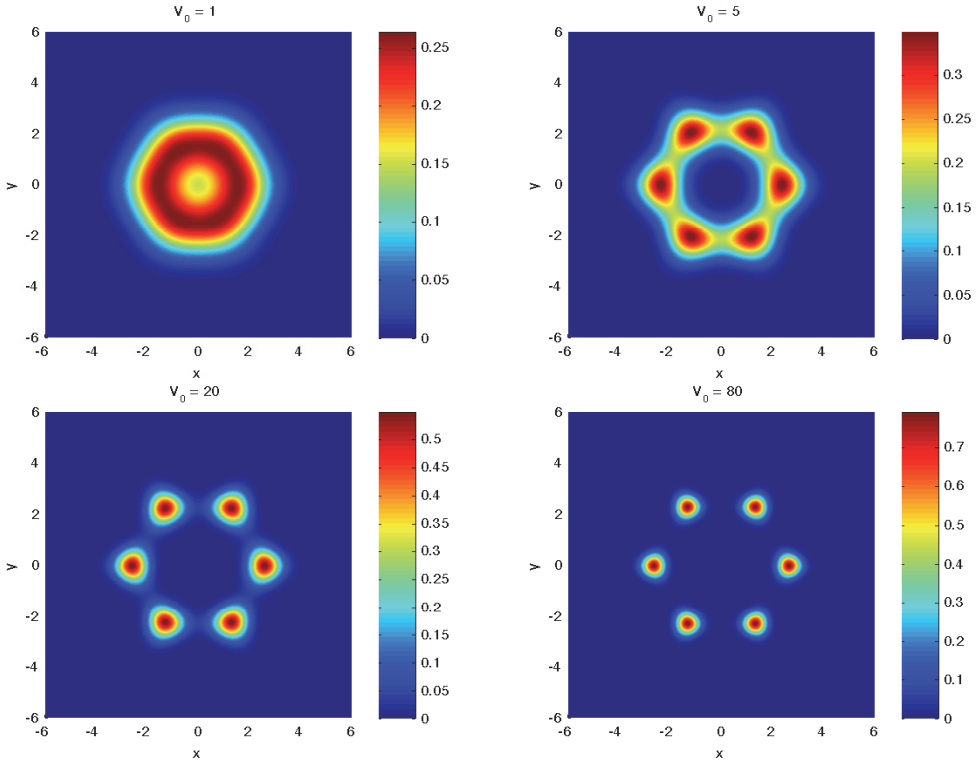

FIG. 4.5. *Contour plots of the ground states of 2D SDM with harmonic + honeycomb potential* (4.2) *for different* V_0 *in section* 4.5.

with $\mathbf{b_1} = \frac{\pi}{4}(\sqrt{3}, 1)$, $\mathbf{b_2} = \frac{\pi}{4}(-\sqrt{3}, 1)$, and V_0 a tunable constant, respectively. Let $\phi_g := \phi_g(x, y)$ be the ground state, which is computed on a computational domain $\Omega = [-16, 16]^2$ with mesh size $h_x = h_y = \frac{1}{16}$. Define the energy $E^g := E(\phi_g)$, kinetic energy $E^g_{\rm kin} := \frac{1}{2}\int_{\mathbb{R}^2} |\nabla\phi_g(\mathbf{x})|^2\,\mathrm{d}\mathbf{x}$, potential energy $E^g_{\rm pot} := \int_{\mathbb{R}^2} V(\mathbf{x})\,|\phi_g(\mathbf{x})|^2\,\mathrm{d}\mathbf{x}$, interaction energy $E^g_{\rm int} := \frac{\beta}{2}\int_{\mathbb{R}^2}(U_2 * |\phi_g|^2)\,|\phi_g(\mathbf{x})|^2\mathrm{d}\mathbf{x}$; variances $\sigma^g_x := \int_{\mathbb{R}^2} x^2|\phi_g(\mathbf{x})|^2\,\mathrm{d}\mathbf{x}$ and $\sigma^g_y := \int_{\mathbb{R}^2} y^2|\phi_g(\mathbf{x})|^2\,\mathrm{d}\mathbf{x}$ in the x- and y-direction, respectively; and density at the origin $\rho_g(\mathbf{0}) := |\phi_g(0,0)|^2$. Table 4.10 lists these quantities of the 2D SDM with harmonic potential (4.1) for different β. In addition, Figure 4.5 depicts the ground states of 2D SDM with $\beta = 5$ and harmonic + honeycomb potential (4.2) for different V_0.

From Table 4.10 and Figure 4.5 as well as additional results not shown here for brevity, for the ground states of the 2D SDM under harmonic potential (4.1),

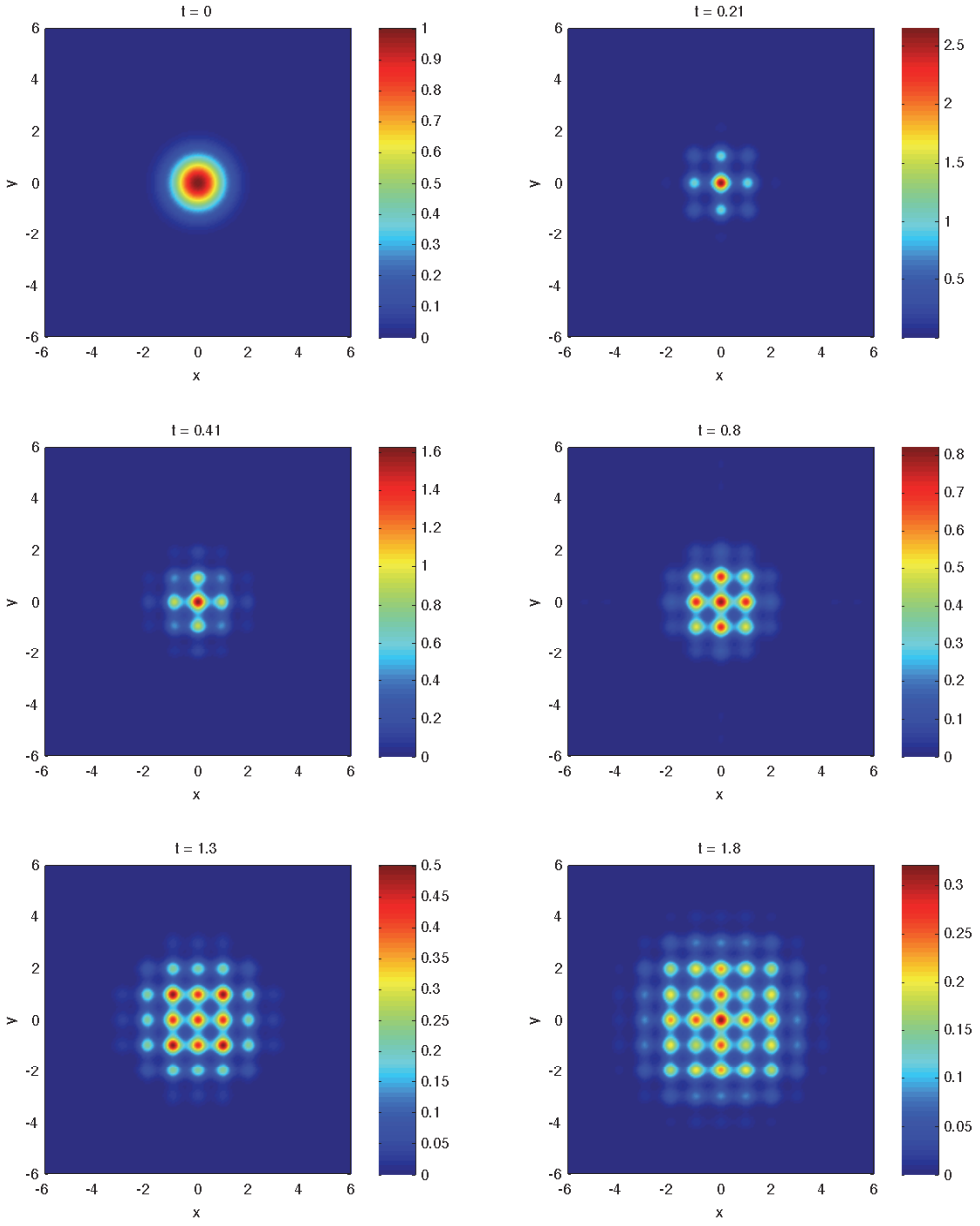

FIG. 4.6. *Time evolution of the density ρ of the 2D SDM with the optical lattice potential* (4.3) *in section* 4.5.

when β increases, the energy, kinetic energy, potential energy, interaction energy, and variances in the x- and y-directions increase, while the density at the origin decreases (cf. Table 4.10). When V_0 becomes larger, the electrons concentrate at the Dirac points of the honeycomb potential (4.2) (cf. Figure 4.5).

For computing the dynamics, we take the initial data in (2.44) as $\psi_0(x, y) =$

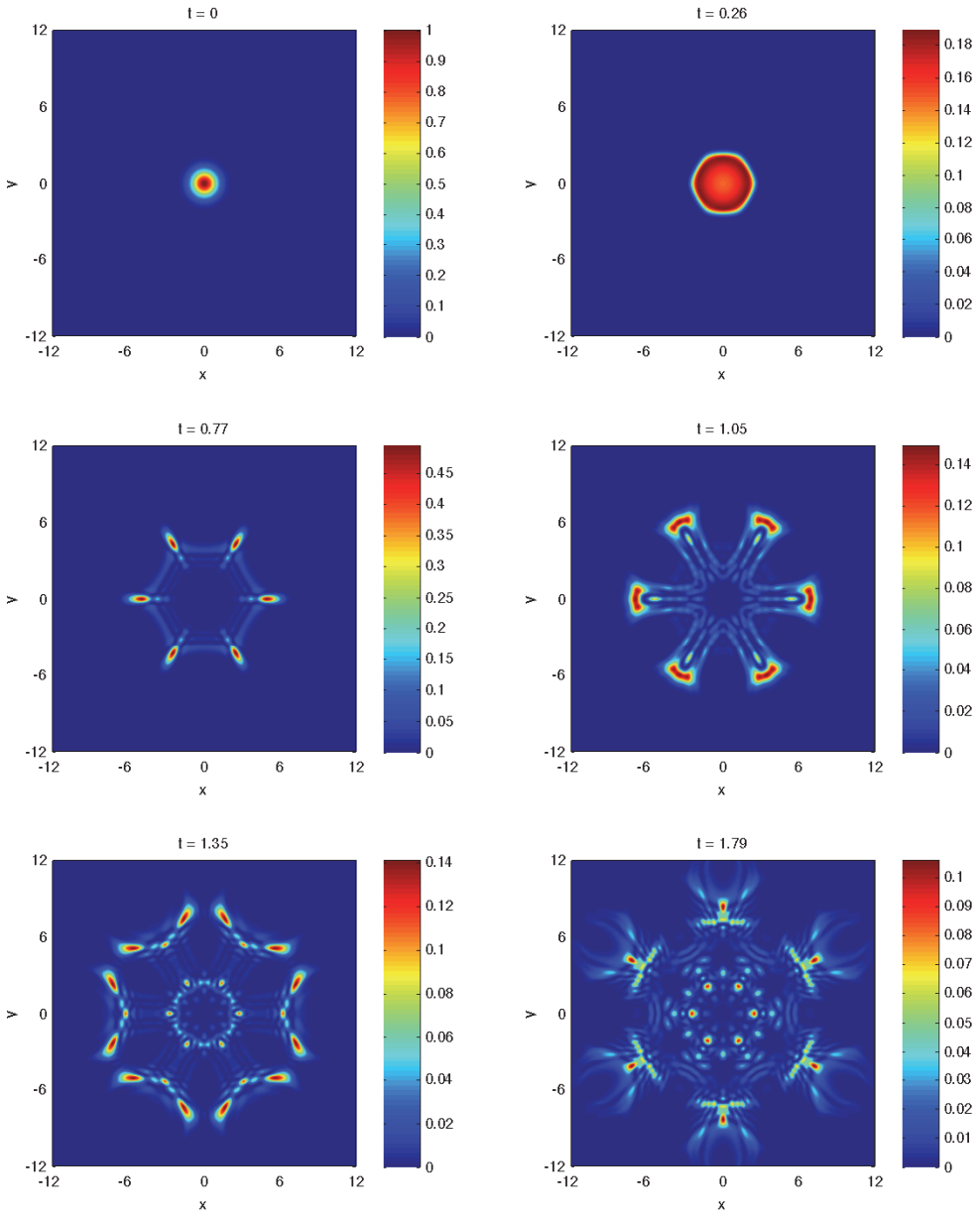

FIG. 4.7. *Time evolution of the density ρ of the 2D SDM with the honeycomb potential* (4.4) *in section* 4.5.

$e^{-(x^2+y^2)/2}$ and consider optical lattice and honeycomb [24] potentials defined as

$$V(x,y) = 10\left[\sin(\pi x)^2 + \sin(\pi y)^2\right], \tag{4.3}$$

$$V(x,y) = 10\left[\cos(\mathbf{b_1}\cdot\mathbf{x}) + \cos(\mathbf{b_2}\cdot\mathbf{x}) + \cos((\mathbf{b_1}+\mathbf{b_2})\cdot\mathbf{x})\right], \tag{4.4}$$

respectively. Let $\psi := \psi(x,y,t)$ be the solution of the 2D SAM which is computed numerically on a computational domain $\Omega = [-16,16]^2$ with mesh sizes $h_x = h_y = \frac{1}{16}$,

and denote the density as $\rho := \rho(x, y, t) = |\psi(x, y, t)|^2$. Figures 4.6 and 4.7 show time evolution of the density ρ of 2D SDM with the optical lattice and honeycomb potentials (4.3) and (4.4), respectively.

From Figures 4.6 and 4.7 and additional results not shown here for brevity, we can see that the 2D SDM describes correct and very interesting dynamics of electrons confined in 2D.

5. Conclusions. We presented how to correctly perform a spatial dimension reduction from the three-dimensional (3D) Schrödinger equation with Coulomb interaction, i.e., the Schrödinger–Poisson system (SPS), under an anisotropic external potential to two dimensions (2D) and one dimension (1D) under strong confinement in the z-direction and (x, y)-plane, respectively. In 2D, we obtained the 2D *surface adiabatic model* (SAM) and *surface density model* (SDM), and, respectively, in 1D, we got the *line adiabatic model* (LAM). Efficient and accurate numerical methods were presented for computing the ground states and dynamics of the 2D SAM and SDM and 1D LAM as well as 2D SPS by focusing on how to evaluate the effective interaction potential efficiently and accurately. Convergence rates were studied and observed numerically in terms of the ground states and dynamics from 3D SPS to 2D SAM and SDM and 1D LAM as well as from 2D SAM to SDM, which confirmed those partial rigorous mathematical results in the literature [17, 18, 19]. Our numerical results provided completed results for all cases. Finally we applied the 2D SDM for studying numerically the ground states and dynamics of electrons confined in the plane under harmonic, optical lattice, and honeycomb potentials. Our results demonstrated that the 2D SDM or SAM describes the correct physics of the ground states and dynamics of electrons confined in 2D, while the 2D SPS might not be a good model in this situation.

Acknowledgment. Part of this work was done when the authors were visiting the Institute for Mathematical Sciences at the National University of Singapore in 2012.

REFERENCES

[1] M. Ali Pourghaderi, W. Magnus, B. Sorée, K. De Meyer, M. Meuris, and M. Heyns, *General 2D Schrödinger-Poisson solver with open boundary conditions for nano-scale CMOS transistors*, J. Comput. Electron., 7 (2008), pp. 475–484.

[2] M. H. Anderson, J. R. Ensher, M. R. Matthewa, C. E. Wieman, and E. A. Cornell, *Observation of Bose-Einstein condensation in a dilute atomic vapor*, Science, 269 (1995), pp. 198–201.

[3] T. Ando, B. Fowler, and F. Stern, *Electronic properties of two-dimensional systems*, Rev. Modern Phys., 54 (1982), pp. 437–672.

[4] W. Bao, N. Ben Abdallah, and Y. Cai, *Gross–Pitaevskii–Poisson equations for dipolar Bose–Einstein condensate with anisotropic confinement*, SIAM J. Math. Anal., 44 (2012), pp. 1713–1741.

[5] W. Bao and Y. Cai, *Mathematical theory and numerical methods for Bose-Einstein condensation*, Kinet. Relat. Mod., 6 (2013), pp. 1–135.

[6] W. Bao, I.-L. Chern, and F. Y. Lim, *Efficient and spectrally accurate numerical methods for computing ground and first excited states in Bose-Einstein condensates*, J. Comput. Phys., 219 (2006), pp. 836–854.

[7] W. Bao and Q. Du, *Computing the ground state solution of Bose–Einstein condensates by a normalized gradient flow*, SIAM J. Sci. Comput., 25 (2004), pp. 1674–1697.

[8] W. Bao, Y. E. Ge, D. Jacksch, and P. A. Markowich, *Convergence rate of dimension reduction in Bose-Einstein condensates*, Comput. Phys. Comm., 177 (2008), pp. 832–850.

[9] W. Bao, D. Jacksch, and P. A. Markowich, *Numerical solution of the Gross-Pitaevskii equation for Bose-Einstein condensation*, J. Comput. Phys., 187 (2003), pp. 318–342.

[10] W. Bao, S. Jin, and P. A. Markowich, *Time-splitting spectral approximations for the Schrödinger equation in the semiclassical regime*, J. Comput. Phys., 175 (2002), pp. 487–524.

[11] W. Bao, S. Jin, and P. A. Markowich, *Numerical study of time-splitting spectral discretizations of nonlinear Schrödinger equations in the semiclassical regime*, SIAM J. Sci. Comput., 25 (2003), pp. 27–64.

[12] W. Bao, N. J. Mauser, and H. P. Stimming, *Effective one particle quantum dynamics of electrons: A numerical study of the Schrödinger-Poisson-Xα model*, Commun. Math. Sci., 1 (2003), pp. 809–831.

[13] C. Bardos, L. Erdős, F. Golse, N. J. Mauser, and H.-T. Yau, *Derivation of the Schrödinger-Poisson equation from the quantum N-particle Coulomb problem*, C. R. Math. Acad. Sci. Paris, 334 (2002), pp. 515–520.

[14] C. Bardos, F. Golse, and N. J. Mauser, *Weak coupling limit of the N-particle Schrödinger equation*, Methods Appl. Anal., 7 (2000), pp. 275–293.

[15] C. Bardos and N. J. Mauser, *The weak coupling limit for systems of $N \to \infty$ quantum particles. State of the art and applications*, J. Soc. Math. Francaise, (2003), pp. 1–14.

[16] G. Bastard, *Wave Mechanics Applied to Semiconductor Heterostructure*, Wiley, New York, 1991.

[17] N. Ben Abdallah, F. Castella, F. Delebecque-Fendt, and F. Méhats, *The strongly confined Schrödinger–Poisson system for the transport of electrons in a nanowire*, SIAM J. Appl. Math., 69 (2009), pp. 1162–1173.

[18] N. Ben Abdallah, F. Castella, and F. Méhats, *Time averaging for the strongly confined nonlinear Schrödinger equation, using almost-periodicity*, J. Differential Equations, 245 (2008), pp. 154–200.

[19] N. Ben Abdallah, F. Méhats, and O. Pinaud, *Adiabatic approximation of the Schrödinger–Poisson system with a partial confinement*, SIAM J. Math. Anal., 36 (2005), pp. 986–1013.

[20] N. Ben Abdallah, F. Méhats, C. Schmeiser, and R. M. Weishäupl, *The nonlinear Schrödinger equation with a strongly anisotropic harmonic potential*, SIAM J. Math. Anal., 37 (2005), pp. 189–199.

[21] X. Cabré and J. Tan, *Positive solutions of nonlinear problems involving the square root of the Laplacian*, Adv. Math., 224 (2010), pp. 2052–2093.

[22] Y. Cai, M. Rosenkranz, Z. Lei, and W. Bao, *Mean-field regime of trapped dipolar Bose-Einstein condensates in one and two dimensions*, Phys. Rev. A, 82 (2010), 043623.

[23] T. Cazenave, *Semilinear Schrödinger Equations*, Courant Lect. Notes Math. 10, Courant Institute of Mathematical Sciences, New York University, New York, AMS, Providence, RI, 2003.

[24] Z. Chen and B. Wu, *Bose-Einstein condensate in a honeycomb optical lattice: Fingerprint of superfluidity at the Dirac point*, Phys. Rev. Lett., 107 (2011), 065301.

[25] P. Choquard, J. Stubbe, and M. Vuffray, *Stationary solutions of the Schrödinger-Newton model: An ODE approach*, Differential Integral Equations, 21 (2008), pp. 665–679.

[26] X. Dong, *A short note on simplified pseudospectral methods for computing ground state and dynamics of spherically symmetric Schrödinger-Poisson-Slater system*, J. Comput. Phys., 230 (2011), pp. 7917–7922.

[27] M. Ehrhardt and A. Zisowsky, *Fast calculation of energy and mass preserving solutions of Schrödinger-Poisson systems on unbounded domains*, J. Comput. Appl. Math., 187 (2006), pp. 1–28.

[28] L. Erdős, B. Schlein, and H.-T. Yau, *Derivation of the Gross-Pitaevskii equation for the dynamics of Bose-Einstein condensate*, Ann. of Math. (2), 172 (2010), pp. 291–370.

[29] L. Erdős and H.-T. Yau, *Derivation of the nonlinear Schrödinger equation from a many body Coulomb system*, Adv. Theor. Math. Phys., 5 (2001), pp. 1169–1205.

[30] H. Fehske, R. Schneider, and A. Weiße, *Computational Many-Particle Physics*, Lecture Notes in Phys. 739, Springer, New York, 2008.

[31] D. K. Ferry and S. M. Goodnick, *Transport in Nanostructures*, Cambridge University Press, Cambridge, UK, 1997.

[32] L. Genovese, T. Deutschb, A. Neelov, S. Goedecker, and G. Beylkin, *Efficient solution of Poisson equation with free boundary conditions*, J. Chem. Phys., 125 (2006), 074105.

[33] Z. Gimbutas, L. Greengard, and M. Minion, *Coulomb interactions on planar structures: Inverting the square root of the Laplacian*, SIAM J. Sci. Comput., 22 (2001), pp. 2093–2108.

[34] P. Harrison, *Quantum Wells, Wires, and Dots: Theoretical and Computational Physics of Semiconductor Nanostructures*, Wiley, Chichester, UK, 2000.

[35] E. H. Lieb and R. Seiringer, *Derivation of the Gross-Pitaevskii equation for rotating Bose*

gases, Comm. Math. Phys., 264 (2006), pp. 505–537.

[36] E. H. Lieb, R. Seiringer, J. P. Solovej, and J. Yngvason, *The Mathematics of the Bose Gas and Its Condensation*, Oberwolfach Semin. 34, Birkhäuser Verlag, Basel, 2005.

[37] E. H. Lieb, R. Seiringer, and J. Yngvason, *Bosons in a trap: A rigorous derivation of the Gross-Pitaevskii energy functional*, Phys. Rev. A, 61 (2000), 043602.

[38] S. Masaki, *Energy solution to a Schrödinger–Poisson system in the two-dimensional whole space*, SIAM J. Math. Anal., 43 (2011), pp. 2719–2731.

[39] F. Méhats, *Analysis of a quantum subband model for the transport of partially confined charged particles*, Monatsh. Math., 147 (2006), pp. 43–73.

[40] O. Pinaud, *Adiabatic approximation of the Schrödinger-Poisson system with a partial confinement: The stationary case*, J. Math. Phys., 45 (2004), pp. 2029–2050.

[41] L. P. Pitaevskii and S. Stringari, *Bose-Einstein Condensation*, Clarendon Press, Oxford, 2003.

[42] E. Polizzi and N. Ben Abdallah, *Self-consistent three-dimensional models for quantum ballistic transport in open systems*, Phys. Rev. A, 66 (2002), 245301.

[43] E. Polizzi and N. Ben Abdallah, *Subband decomposition approach for the simulation of quantum electron transport in nanostructures*, J. Comput. Phys., 202 (2005), pp. 150–180.

[44] M. Rosenkranz, Y. Cai, and W. Bao, *Effective dipole-dipole interactions in multilayered dipolar Bose-Einstein condensates*, Phys. Rev. A, 88 (2013), 013616.

[45] Ó. Sánchez and J. Soler, *Long-time dynamics of the Schrödinger-Poisson-Slater systems*, J. Statist. Phys., 114 (2004), pp. 179–204.

[46] J. Shen and T. Tang, *Spectral and High-Order Methods with Applications*, Science Press, Beijing, 2006.

[47] G. Strang, *On the construction and comparison of difference schemes*, SIAM J. Numer. Anal., 5 (1968), pp. 506–517.

[48] N. Yarvin and V. Rokhlin, *An improved fast multipole algorithm for potential fields on the line*, SIAM J. Numer. Anal., 36 (1999), pp. 629–666.

[49] H. Yoshida, *Construction of higher order symplectic integrators*, Phys. Lett. A, 150 (1990), pp. 262–268.

[50] Y. Zhang and X. Dong, *On the computation of ground state and dynamics of Schrödinger-Poisson-Slater system*, J. Comput. Phys., 230 (2011), pp. 2660–2676.